The MAVEN Magnetic Field Investigation

J. E. P. Connerney, J. Espley, P. Lawton, S. Murphy,
J. Odom, R. Oliversen, and D. Sheppard

NASA Goddard Space Flight Center
Solar System Exploration Division
Planetary Magnetospheres Laboratory
Greenbelt, MD 20771

November 1, 2014

Corresponding author: J. Connerney
Email: jack.connerney@nasa.gov
Phone: 301-286-5884
Fax no: 301-286-3346

Abstract: The MAVEN magnetic field investigation is part of a comprehensive particles and fields subsystem that will measure the magnetic and electric fields and plasma environment of Mars and its interaction with the solar wind. The magnetic field instrumentation consists of two independent tri-axial fluxgate magnetometer sensors, remotely mounted at the outer extremity of the two solar arrays on small extensions ("boomlets"). The sensors are controlled by independent and functionally identical electronics assemblies that are integrated within the particles and fields subsystem and draw their power from redundant power supplies within that system. Each magnetometer measures the ambient vector magnetic field over a wide dynamic range (to 65,536 nT per axis) with a quantization uncertainty of 0.008 nT in the most sensitive dynamic range and an accuracy of better than 0.05%. Both magnetometers sample the ambient magnetic field at an intrinsic sample rate of 32 vector samples per second. Telemetry is transferred from each magnetometer to the particles and fields package once per second and subsequently passed to the spacecraft after some reformatting. The magnetic field data volume may be reduced by averaging and decimation, when necessary to meet telemetry allocations, and application of data compression, utilizing a lossless 8-bit differencing scheme. The MAVEN magnetic field experiment may be reconfigured in flight to meet unanticipated needs and is fully hardware redundant. A spacecraft magnetic control program was implemented to provide a magnetically clean environment for the magnetic sensors and the MAVEN mission plan provides for occasional spacecraft maneuvers – multiple rotations about the spacecraft x and z axes – to characterize spacecraft fields and/or instrument offsets in flight.

I)   Introduction

The Mars Atmosphere and Volatile EvolutioN (MAVEN) mission seeks to understand the history of climate change on Mars by studying the present state of the Mars upper atmosphere and ionosphere, and the processes governing atmospheric loss to space [*Jakosky et al.,* 2014]. Mars has a thin and dusty atmosphere comprised primarily of carbon dioxide (96%), argon (~2%) and nitrogen (~2%) with traces of carbon monoxide, water, oxygen, and other gases. The temperatures and pressures in the Mars lower atmosphere are comparable to those found in the Earth's stratosphere. With a surface pressure of only about 1% of Earth's, and temperatures well below 273 K, it is difficult to reconcile the thin atmosphere we see today with the geological evidence (channels, valley networks, erosional features, small scale layering, and aqueous mineralogy) that suggest water flowed on Mars until about 4 billion years ago.

The preponderance of geologic evidence suggests that early Mars had a warm and dense atmosphere and perhaps an ocean, if not standing water, persisting for a geologically significant period. If so, where is this water today, and what became of the dense atmosphere? Mars is not so massive as to trap volatile species indefinitely, so while loss processes remain poorly understood, atmospheric loss to space is a prime candidate for their removal. Indeed, ample evidence of an enrichment of heavy isotopes ($^{15}N/^{14}N$, $^{38}Ar/^{36}Ar$, and D/H) in the atmosphere [*Jakosky and Phillips*, 2001; *Mahaffy et al.,* 2013] and direct measurements of escaping ions made by orbiting spacecraft [*Barabash et al.*, 2007; *Nilsson et al.*, 2011] implicate loss to space as a significant, if not dominant, loss mechanism throughout Mars history.

The Mars atmosphere no longer enjoys the protection from the solar wind afforded by the presence of a global magnetic field of appreciable magnitude. However, early Mars did have an Earth-like magnetic field of sufficient strength to shelter the atmosphere from the solar wind [*Acuña et al.*, 1998; 1999; 2001]. So it is tempting to speculate that a warm and dense Mars atmosphere existed within the protection afforded by an early Mars dynamo, and the demise of the dynamo, some 4 billion years ago, exposed the atmosphere to stripping by the solar wind. Had Mars retained a dynamo, would it be more habitable today? To answer this question we need understand the processes at work in the Mars atmosphere, and how to use that knowledge to infer the evolutionary

76   history of the atmosphere. There is also evidence for sequestration of water and possibly other

77   volatiles in the Mars regolith, especially at mid and high latitudes.

78

79   The MAVEN spacecraft will spend more than a Mars year in polar orbit, sampling the Mars space

80   environment with a full suite of in-situ and remote sensing instruments [*Jakosky et al.*, 2014]. These

81   instruments are designed to provide the measurements necessary to characterize the upper

82   atmosphere and ionosphere; quantify the current rate of escape of atmospheric constituents under a

83   variety of solar wind conditions; and by backward extrapolation (more accurately, modeling)

84   quantify the total atmospheric loss to space throughout Mars history. In looking back through time,

85   we must bear in mind that our young Sun was likely far more active than at present, characterized

86   by dramatically more violent outflows than we see today. The MAVEN prime mission is designed

87   to observe the solar wind interaction with Mars during the declining phase of the current solar cycle,

88   which thus far appears unremarkable but for a relatively weak sunspot activity.

89

90
91
92   II)   Science Objectives

93
94   a.   Mars Magnetic Field

95
96   The discovery of the intense magnetization of the Mars crust is one of the most remarkable findings of

97   the exploration of Mars, and one of the most illuminating. The Mars Global Surveyor (MGS) mission

98   established that Mars has no global magnetic field, and therefore no dynamo at present, but it must have

99   had one in the past when the crust acquired intense remanent magnetization. It is likely that a molten

100 iron core formed early, after or during hot accretion 4.5-4.6 Ga, and for at least a few hundred million

101 years a substantial global field was generated by dynamo action in the core. The chronology proposed

102 by *Acuña et al.* [1999] attributes the global distribution of magnetization to the early demise of the

103 dynamo, prior to the last great impacts (~4 Ga) that left large unmagnetized basins in the crust. This

104 view has been supported by more complete analyses of the large impact basins [*Lillis et al.*, 2008; *Lillis*

105 *et al.*, 2013], leading to more precise estimates of the dynamo's demise. It appears that dynamo

106 generation of the global magnetic field was extinguished before formation of Hellas and Utopia basins

107 approximately 4.0-4.1 Ga.

108

109 Early onset and cessation of the dynamo is difficult to reconcile with the notion of a dynamo driven by

110 solidification of an inner core [*Schubert et al.,* 1992], the preferred energy source for the Earth's

111 dynamo. Alternatively, an early dynamo can be driven by thermal convection, with or without plate

112 tectonics, for the first 0.5 – 1 Gyr [*Breuer and Spohn*, 2003; *Schubert and Spohn*, 1990; *Stevenson et al.,*

113 1983; *Connerney et al.*, 2004], persisting as long as the core heat flow remains above a critical threshold

114 for thermal convection [*Nimmo and Stevenson*, 2000]. With knowledge that Mars had a substantial

115 global magnetic field billions of years ago, it is quite natural to consider whether the Mars atmosphere

116 may have been sheltered from the solar wind for a geologically significant period. In the dynamo era,

117 Mars may have retained a warm and dense atmosphere, only to lose it subsequent to decay of the global

118 field. Did the Mars dynamo prevent loss of atmosphere to space?

119

120 There is also a supply side argument to be made on behalf of the Mars dynamo, if only indirectly. The

121 supply side argument follows from interpretation of the crustal magnetic imprint within the framework

122 of plate tectonics. A planetary dynamo is driven by vigorous convective motions in the core, resulting

123 from a temperature gradient across the core-mantle boundary. The thermal gradient persists as long as an

124 efficient cooling mechanism (e.g., mantle convection, and plate tectonics) is maintained. Following this

125 line of thought, the demise of the dynamo may be associated with cessation of plate tectonics. On earth,

126 we associate plate tectonics with active geological processes: crustal subduction, mantle convection,

127 active volcanism, and consequently venting of gases from the interior. This is the rationale for a supply

128 side argument: maintenance of a dense atmosphere via the active geologic processes associated with

129 mantle convection, subduction, and volcanism.

130

131 After more than 2 full Mars years of mapping operations, MGS produced an unprecedented global map

132 of magnetic fields produced by remanent magnetism in the crust. This map (**Figure 1**) reveals contrasts

133 in magnetization that appear in association with known faults; variations in magnetization clearly

134 associated with volcanic provinces; and magnetic field patterns reminiscent of transform faults at

135 spreading centers [*Connerney et al,* 2005]. *Connerney et al.* proposed that the entire crust acquired a

136 magnetic imprint via crustal spreading and cooling in the presence of a reversing dynamo; and that

137 erasure of this imprint occurred where the crust was buried (thermal demagnetization) by flood basalts

138 to depths of a few km. Transform faults are unique to plate tectonics, so if these features are indeed

4

139 transform faults then the Mars crust formed via sea floor spreading as on Earth [*Connerney et al.,* 1999;

140 *Sleep,* 1990].

141

142 The magnetic record is complemented by geomorphological analyses that are suggestive of plate

143 tectonics having occurred on Mars early in its history. The alignment of the great volcanic edifices on

144 Mars is consistent with plate motion over a mantle plume [*Connerney et al.*, 2005] or, conversely,

145 volcanic chains formed above subducting slabs [*Sleep,* 1990 ; *Sleep,* 1994; *Yin, personal*

146 *communication*, 2012]. The topographical relief along much of the dichotomy boundary has been

147 interpreted as a series of ridge/transform fault segments [*Sleep*, 1994]. A recent structural analysis of the

148 Valles Marineris fault zone [*Yin,* 2012] likens this trough system to the left-slip, transtensional Dead Sea

149 fault zone on Earth: an undisputed plate boundary. It is difficult to understand how such a structure

150 evolved on Mars in the absence of plate tectonics.

151

152 Is it possible that a warm and dense atmosphere on Mars was supplied by outgassing associated with

153 plate tectonics? If so, the Mars dynamo may have been instrumental in both the supply and maintenance

154 of an early dense atmosphere. The fate of Mars' atmosphere may well be inseparable from cessation of

155 plate tectonics and the demise of the dynamo; a marker for the evolution of Mars as a planet.

156
157   b.   Interaction with the Solar Wind
158
159 Mars stands as an obstacle to the *solar wind*, the high velocity (supersonic) stream of plasma emanating

160 from the sun. The expanding solar wind drags the frozen-in *interplanetary magnetic field* (IMF) along

161 with it, and forms a multi-tiered interaction region about Mars as it interacts with the extended

162 atmosphere and electrically-conducting conducting ionosphere (**Figure 2**). The characteristics of the

163 solar wind interaction with a weakly magnetized, or unmagnetized body are in some regards similar to

164 the flow about a magnetized planet [*Luhmann et al,* 1992; *Brain*, 2006], but for the lack of a global-scale

165 *magnetosphere* within which the motion of charged particles is governed by an intrinsic planetary

166 magnetic field.

167

168 Since the solar wind is supersonic, a *bow shock* forms upstream of Mars (**Figure 2**). The slowed,

169 shocked solar wind flows around the obstacle within the *magnetosheath*, a turbulent region [*Espley et*

170 *al*., 2004] bounded by the bow shock and a lower boundary, often referred to as the *magnetic pile-up*

171 *boundary* [*Bertucci et al.,* 2003], or alternatively the *induced magnetosphere boundary* [e.g., *Brain et*

172 *al*., 2015] or *induced magnetopause*. It marks the narrow transition between plasma dominated by ions

173 of solar wind origin and plasma dominated by ions of planetary origin; it is often approximated by a

174 paraboloid of revolution about the planet-sun line. The magnetic field extends well downstream in the

175 anti-sunward direction, in effect draped around the conducting obstacle, to form the *magnetotail*, by

176 analogy with the magnetotail that forms downstream of a magnetic planet. A magnetic planet imposes a

177 geometry and polarity on the field in its magnetotail, whereas the magnetotail formed downstream of an

178 unmagnetized body changes direction in response to changes in the direction of the interplanetary

179 magnetic field.

180

181 However, Mars is neither an unmagnetized body, such as Venus, nor a magnetized body, like Earth.

182 Where the Mars crust is intensely magnetized it can establish order over scale lengths of hundreds of

183 kilometers much in the way the Earth's field does. In the Earth's upper atmosphere and ionosphere, a

184 complex system of currents flow in response to solar heating of the atmosphere, particularly where

185 horizontal magnetic fields are encountered (equatorial fountain effect and electrojet), and in response to

186 the imposition of electric potentials (in particular, auroral ovals). By analogy to magnetized planets,

187 field-aligned currents, called *Birkeland currents*, flow along the magnetic field and deposit energy into

188 the electrically conducting ionosphere, particularly during solar storms, leading to auroral displays.

189 Auroral emissions have been observed on Mars [*Bertaux et al.,* 2005; *Brain et al.,* 2006; *Lundin et al.,*

190 2006; *Brain and Halekas*, 2012.] in association with the most intensely magnetized regions of the

191 southern highlands. On earth, and other planets with (dipolar) magnetic fields, auroral displays are most

192 often observed in the polar regions. In contrast, on Mars, auroral emissions are observed in association

193 with intense crustal magnetic fields that are strong enough to sustain magnetic fields to great heights,

194 well above the ionosphere. **Figure 3** illustrates the complexity of the magnetic field observed in a

195 meridian plane projection over the southern highlands, extending throughout the Mars upper atmosphere

196 and ionosphere. The MAVEN spacecraft will sample the magnetic field and plasma environment

197 throughout this region from about 120 km upwards, during "deep dip" campaigns and nominal orbital

198 operations.

199

200 The crustal fields are strong enough to dramatically alter the nature of the interaction with the solar

201 wind, as can be seen in the multi-fluid magnetohydrodynamic simulation [*Dong et al., 2014*] illustrated

202   in **Figure 4**. Field magnitudes are appreciably larger in regions of strong crustal fields than they would

203   otherwise be, creating "mini-magnetospheres" where charged particle motion is guided by persistent,

204   and stable, magnetic geometries. The geometry imposed by strong crustal fields dictates where field

205   lines threading the ionosphere link with the solar wind and distant plasma environments, giving rise to

206   deposition of energy and aurorae. The strong crustal fields can also impose a polarity and geometry in

207   the magnetotail as they are drawn tailward by the solar wind [*Brain et al.*, 2010]. Numerical simulations

208   have amply demonstrated that the strong magnetic fields associated with the southern highlands have a

209   shielding effect that reduces the ion escape flux [*Ma et al*, 2004; *Dong et al.*, 2014].

210

211   In collisionless plasmas, waves provide one of the main ways of distributing energy across the system.

212   Ion cyclotron waves are produced when ions move in resonance with the magnetic fields. This produces

213   fluctuations in the magnetic field with frequencies that depend on the mass and charge state of the ions

214   producing them. Additionally, the highly turbulent Martian magnetosheath offers an unusual plasma

215   environment where nonlinear (i.e. $\delta B \sim |B|$) kinetic plasma modes develop [*Glassmeier and Espley*,

216   2006]. Some groups have examined the role that plasma wave heating may play in the escape of

217   atmosphere [*Ergun et al.,* 2006; *Andersson et al.,* 2010] but this task will be easier once the full

218   Poynting flux is available using data from both the MAVEN MAG and LPW instruments.

219

220   *Magnetic reconnection* is another important plasma process that may play an important role in bulk

221   atmospheric escape [*Brain et al.,* 2010]. Magnetic reconnection may occur when anti-parallel (or nearly

222   so) magnetic fields are brought together in a plasma, resulting in a localized exception to the frozen-in

223   condition of the magnetic field. This allows magnetic fields to reconfigure ("reconnect") and in the

224   process magnetic energy is converted into thermal energy. Energization of the plasma can enhance

225   atmospheric escape but the geometrical consequences of reconnection could be at least as important.

226   The reconfiguration of the magnetic field may allow field lines that were connected to the IMF to lose

227   that connection; conversely, reconfiguration may at times facilitate continuity with the IMF. *Halekas et*

228   *al.* [2009] found many observations indicative of reconnection at Mars, suggesting that reconnection

229   may not be uncommon. The first of its kind, fully instrumented particles and fields package (PFP)

230   onboard MAVEN will allow careful investigation of this possibility.

231

232 The measurement of magnetic fields at Mars is therefore important to a variety of interrelated scientific

233 topics, all bearing on the processes that control atmospheric loss to space. Characterizing the magnetic

234 fields throughout the interaction region provides an interpretative framework to help us understand the

235 complicated hybrid induced-crustal magnetosphere. In addition, the magnetic field magnitude and

236 geometry are critical for understanding the trajectories of potentially escaping charged particles. The

237 MAVEN Magnetic Fields Investigation plays an important role in understanding the role of plasma

238 waves, reconnection, and bulk plasma structures in facilitating atmospheric escape and more broadly in

239 the dynamics of the solar wind interaction.

240

241

242
243 III)   Science Requirements
244
245 The magnetometer investigation (MAG) driving requirements benefit from a detailed knowledge of

246 the magnetic field environment that MAVEN will transit, a consequence of the Mars Global

247 Surveyor magnetic mapping. The MAVEN MAG requirements are sourced from the MAVEN

248 Mission Requirements Document (MAVEN-PM-RQMT-0005), the MAVEN Level 3 Functional

249 Requirements – Particle & Fields Functional Requirements Document (MAVEN-PFIS-RQMT-

250 0016), and the MAVEN Magnetometer Level 4 Functional Requirements Document (MAVEN-

251 MAG-RQMT-0061). The instrument requirements as follows:

252
253 • Measure the magnitude and direction of the ambient magnetic field;

254 • Provide the vector magnetic field (broadcast vector) to other science payloads in flight;

255 • Encompass a dynamic range of measurement from 3 nT to 3000 nT;

256 • Measurement accuracy & resolution of 1% or better;

257 • Sample rate providing temporal resolution of 20 seconds or better;

258 • Provide complete hardware redundancy of magnetic field measurement;

259 • Sensor orthogonality and alignment knowledge to 0.25 degrees or better;

260 • Provide non-magnetic a/c heaters for sensor thermal control, operating and non-operating.

261

Magnetometer Sensor Performance	
Sensor type	Dual tri-axial ring core fluxgates
Accuracy	0.05% absolute vector accuracy
Intrinsic noise level	0.015 nT (most sensitive range)
Attitude knowledge	Better than 0.05 degrees
Zero level stability	< 1 nT
Dynamic ranges (resolution)	512 nT ($\pm$ 0.015 NT) 2048 nT ($\pm$ 0.062 nT) 65536 nT ($\pm$ 2.0 nT)
Intrinsic sample rate	32 vector samples/second
Radiation total ionizing dose (TID)	> 50 krad (at component level)

262

263
264
265
266 A more complete study of the magnetic field magnitudes that MAVEN may sample, between target

267 altitudes of 125 and 400 km, was performed to optimize the choice of instrument dynamic ranges.

268 Since MAVEN's mission plan does not target specific latitudes/longitudes, we need be prepared for

269 the maximum field magnitude that might be experienced above the surface of the planet at altitudes

270 in excess of ~100 km. This study demonstrated that it is very unlikely that a dynamic range of 512

271 nT might be exceeded throughout the entire mission, including the "deep dip" orbits. The

272 magnetometer system provided as part of the Particles and Fields Package meets and exceeds the

273 Project requirements with a pair of independent magnetic sensors with the following performance

274 characteristics:

275

276
277 IV)   Investigation Design and Spacecraft Accommodation
278
279   a. Investigation Design
280
281 The MAVEN particles and fields instrumentation form an ensemble of instruments ("Particles and

282 Fields Package") controlled by a single hardware-redundant data processing unit (PFDPU)

283 interfacing to the spacecraft. The PFP (**Figure 5**) services the Solar Wind Electron Analyzer

284 (SWEA) instrument [*Mitchell et al.,* 2014], the Solar Wind Ion Analyzer (SWIA) instrument

285 [*Halekas et al*., 2014], the Langmuir Probe and Waves (LPW) instrument [*Andersson et al.,* 2014],

286 the Extreme Ultraviolet (EUV) instrument, the Solar Energetic Particles (SEP) instrument, and the

287 (STATIC) instrument [*McFadden et al.,* 2014] in addition to the Magnetometer instrumentation

288 (MAG). The MAVEN magnetic field investigation (MAG) consists of two independent and

289 identical fluxgate magnetometer systems that are interfaced to and controlled by the PFDPU. The

290 particles and fields electronics package is a stack of individual electronics boxes (**Figure 6**) that

291 service each of the instruments; two of the "slices" are occupied by identical magnetometer

292 electronics frames that service the two magnetometer sensors. Each electronics box is fully shielded

293 and each draws power from the redundant power supplies within the PFP.

294

295 Individual and independent a/c heater electronics assemblies provide thermal control for the MAG

296 sensors and are also accommodated on separate cards elsewhere within the PFP. These are powered

297 directly by the spacecraft, providing uninterruptable power for sensor thermal control regardless of

298 the state (on or off) of the PFP. The a/c heaters are proportional controllers that maintain sensor

299 temperature within comfortable operational limits. They are designed to insure that no dc currents

300 can circulate in the resistive heater elements that are placed underneath the sensor base and within

301 the sensor thermal blanketing. (The spacecraft heaters are direct current powered and are therefore

302 not suitable for use in proximity with a magnetic sensor).

303

304 The magnetometer sensors are located at the very end of the solar array panels on modest

305 extensions (.66 m in length) designated as MAG "boomlets", placing them approximately 5.6 m

306 from the center of the spacecraft body (**Figure 7**). Magnetometer sensors are best accommodated

307 remotely, as far from spacecraft subsystems as is practical, to minimize the relative contribution of

308 spacecraft-generated magnetic fields. Care is taken to minimize the magnetic signature of spacecraft

309 subsystems, of course, but one of the most effective ways to reduce spacecraft-generated magnetic

310 fields is to separate spacecraft systems and sensor, taking maximum advantage of the $1/r^3$

311 diminution of a magnetic (dipole) source with distance from the source. Thus magnetometer sensors

312 are often accommodated on a lengthy dedicated magnetometer boom that is deployed after launch.

313 Alternatively, they may be accommodated at the outer extremity of the solar arrays, taking

314 advantage of an essential appendage that also deploys post-launch. MAVEN took the latter

315 approach, much as its predecessor Mars Global Surveyor did [*Acuña et al.*, 2001].

316

317 In typical implementations, a pair of magnetic sensors ("dual magnetometer technique") provides

318 hardware redundancy as well as a capability to detect magnetic fields at two locations on the

319 spacecraft. This capability offers the potential to monitor spacecraft generated magnetic fields in

320 flight, by comparison of the field measured by each sensor. When both sensors are mounted along a

321 radius vector on a dedicated magnetometer boom, one "outboard" and one "inboard", one can take

322 advantage of the $1/r^3$ diminution of the (dipolar) field of the spacecraft with distance along the

323 boom to identify local sources and separate the fields due to local sources from the ambient field.

324 The outboard sensor is typically allocated the majority of the spacecraft telemetry allocation for the

325 investigation, and sampled at a higher rate than the inboard sensor, anticipating a spacecraft field

326 that changes slowly in time (this is not always the case!). Thus the outboard sensor is the primary

327 sensor, and the inboard sensor is the secondary sensor, though in many implementations their role

328 may be reversed if desired.

329
330 The MAVEN magnetometer sensors are located on the +Y spacecraft solar array ("outboard") and

331 the –Y spacecraft solar array ("inboard"). The assignment is arbitrary, and in keeping with prior

332 missions (Mars Observer, Mars Global Surveyor) and software heritage; you may prefer to think of

333 the +Y sensor as the primary sensor, and –Y as the secondary sensor. In reality, they are identical,

334 and each sensor is capable of performing either role. It was anticipated that the +Y sensor

335 ("outboard" or primary sensor) location would be preferred over the –Y sensor location, from a

336 spacecraft magnetic interference perspective, by virtue of the location of various components on the

337 body of the spacecraft (reaction wheels in particular). Thus the +Y sensor was designated as

338 primary sensor ("outboard"), and –Y sensor as secondary sensor; observations of the magnetic field

339 during cruise operations confirmed this expectation. In early cruise, the inboard or secondary

340 sensor was sampled at a lesser rate, but as of June 2014, our current practice is to utilize the same

341 sample rate for both sensors for diagnostic purposes.

342

343   b. Spacecraft Requirements

344

345 Instrument accommodation is always of concern for a magnetometer investigation, extending

346 beyond the mechanical and thermal interfaces discussed above. Since the magnetometer sensors

347 measure the ambient magnetic field, any appreciable spacecraft-generated magnetic fields may

348 interfere with accurate measurement of the environmental field. The magnetic field produced by the

349 spacecraft is managed via a spacecraft magnetic control plan that tracks the expected magnetic field

350 at the sensor locations, and manages the net field at the sensors to meet a requirement appropriate to

351 the mission. In recognition of the relatively weak field of the solar wind at Mars, the Project

352 adopted a spacecraft magnetic field requirement not to exceed (NTE) 2 nT static and 0.25 nT

353 variable. The static field is allocated a larger limit because with periodic spacecraft maneuvers a

354 static magnetic field may be measured and corrected analytically.

355

356

357   c. Spacecraft Magnetic Control Plan

358

359 During the spacecraft design phase, and through assembly, test, and launch operations (ATLO), a

360 magnetic model of the spacecraft was maintained as part of the spacecraft magnetic control

361 program. This model accounts for the location and magnetic moment of spacecraft components and

362 subsystems, and provides an estimate of the resultant spacecraft magnetic field, summed vectorially

363 over its many parts, at the magnetometer sensor locations. The model is used to help allocate a

364 fraction of the total NTE requirement to various subsystems and to guide mitigation where

365 necessary. For example, when preliminary magnetic testing of the reaction wheel assemblies

366 (RWA) indicated that they would contribute excessively to the variable (ac) spacecraft field, the

367 Project responded with magnetic shielding enclosures for the RWAs that lessened their contribution

368 by about an order of magnitude.

369

Spacecraft components, subsystems, and instruments were characterized by magnetic test at the Lockheed Martin Waterton Canyon facility or at subcontractor facilities. Test articles included engineering models that were available early in the program and for some subsystems and instruments, flight or qualification models. The solar arrays were carefully designed with compensation loops to null the magnetic signature of the array under illumination. This was accomplished by compensating each individual cell string with a matched compensation loop on the underside of the panel ("backwiring"). Verification testing of the solar array compensation scheme was performed on a qualification panel tested at LM's Sunnyvale facility. This test consists of exciting the compensated string with a square-wave current and measurement of the resultant magnetic field with a magnetic gradiometer, using synchronous detection to accurately determine the response in an industrial environment. The actual flight arrays did not receive active magnetic testing although the arrays and array extensions ("boomlets") did undergo magnetic screening (with a sensitive magnetic gradiometer) for magnetic remanence (magnetic "sniff test"). This testing is done on the flight article, and any objects (hardware, thermal blankets, etc.) installed near the end of the array, to avoid magnetic contamination near the sensor.

The entire spacecraft underwent additional testing prior to shipment to the launch site. One test ("swing test") was performed to provide an estimate of the net spacecraft magnetic moment, and another ("magnetic compatibility test") was performed to measure the magnetic field produced by systems and components when activated. The swing test, as the name implies, consists of measuring the variation in magnetic field observed by a static magnetic sensor as the spacecraft, suspended at the end of a lanyard, executed pendulum motion. This motion provides a clear periodic signal that is easily distinguished from background in an industrial facility. A rotation test was also performed, in which the suspended spacecraft was rotated in the presence of the magnetic sensor, to identify the location of magnetically "hot" components. For the magnetic compatibility test, the magnetic field was monitored as various subsystems were energized, to characterize the resultant magnetic signature. During one of these tests, we identified dc heaters in the propulsion system that had not been compensated properly; Project was able to reconfigure the operation of these heater circuits prior to shipment to reduce the stray field to acceptable levels.

V)   Fluxgate Magnetometer

402   a.   Instrument Description

403

404   The GSFC fluxgate magnetometer meets and exceeds the vector measurement requirement with a

405   simple and robust instrument with extensive flight heritage. The MAVEN magnetometer design

406   draws from Goddard's extensive flight experience, with over 78 magnetometers developed for

407   space research and built at GSFC (e.g., Voyagers 1 and 2, Pioneer 11, Giotto, Lunar Prospector,

408   Mars Observer, Mars Global Surveyor, MESSENGER, STEREO, WIND, ACE, AMPTE, TRMM,

409   Freja, Viking, UARS, DMSP, Firewheel, MAGSAT, POGS, RBSP, and Juno). All are based on

410   fluxgate designs developed by Mario Acuña at GSFC. The MAVEN sensors cover the modest

411   dynamic range requirement with two instrument ranges that will be used in the Mars environment

412   (+/- 512 nT and +/- 2048 nT full scale). The instrument also has a high range (65,536 nT full scale)

413   that is useful in integration and test, permitting operation in ambient field in an Earth field

414   environment without resort to magnetic shielding or nulling devices.

415

416   i.   Principle of Operation

417

418   The fluxgate magnetometer is a simple, robust sensor capable of very high vector accuracy while

419   requiring only modest resources [*Acuña*, 2002]. The principle of operation is illustrated with the

420   help of the simplified schematic (**Figure 8**) that describes a generic, single axis fluxgate

421   magnetometer utilizing a ring core sensing element. The sensing element is a high permeability ring

422   formed by wrapping a thin tape of 6-81 molybdenum permalloy onto a non-magnetic Inconel hub.

423   This material is nickel-iron alloy with about 81% nickel and 6% molybdenum content, the

424   remainder iron, with a magnetic permeability of order 100,000.

425

426   The "fluxgate" works by driving this sensing element cyclically into saturation by exciting a

427   toroidal winding at a drive frequency, typically about 15 kHz. The core saturation "gates" the

428   ambient magnetic flux threading the sensing coil, as the core permeability alternates between very

429   high, in the unsaturated state, and very low, in the saturated state. Core saturation occurs at twice

430   the drive frequency, modulating the ambient flux at twice the drive frequency, and inducing a

431   voltage in the sensing coil at 2f, which is amplified and passed to a synchronous detector. The

432   synchronous detector is essentially a lock-in amplifier, using as a reference the second harmonic of

433   the drive frequency, all derived from a stable crystal controlled oscillator. The output of the detector

434   is fed back to the sense coil to drive the field in the sensor to zero, which results in a sensor with

435   very high linearity. The output voltage is linearly related to the ambient field aligned with the axis

436   of the sense/feedback coil. Several dynamic ranges may be implemented by selection of different

437   feedback resistors using field effect transistors to perform the switching function.

438

439   A vector instrument (**Figure 9**) incorporates three single axis analog circuits like that shown

440   schematically in **Figure 8**, or possibly four if a redundant axis is included. The three component (x,

441   y, z) analog outputs are sampled by dedicated 16-bit Analog-to-Digital Converters (ADC) which are

442   controlled by, and read by, a digital processor that formats the data for transfer to the PFPDPU,

443   along with housekeeping data (temperatures, voltages, current measurements).

444

445   The MAVEN sensor (**Figure 10 and 11**) utilizes two ring core sensing elements, each of which sits

446   inside of a pair of nested sense/feedback coils. This design uses the pair of orthogonal

447   sense/feedback coils to detect both components of the magnetic field in the plane of the ring core,

448   and to null the field in the plane of the ring core. Since each sensor element measures the field in

449   two orthogonal directions, one may either have a redundant measure of the field along one axis or

450   one may simply drive the redundant sense/feedback coil to null with the output from the companion

451   sensor. The MAVEN magnetometers use this approach to null the field along the redundant axis.

452   This design achieves superior linearity in strong fields relative to designs using single axis

453   sense/feedback coils and it uses only two ring core sensing elements instead of the three required

454   for a vector instrument otherwise. Each sensor assembly (**Figure 12**) is permanently mated to an

455   optical cube that defines the reference coordinate system for the sensor.

456

457   ii.   Analog Design

458

459   The FGM electronics (analog and digital) for each magnetometer are mounted in a single card

460   frame in the PFP stack (**Figure 13**). The thermal controllers for the sensors are mounted back-to-

461   back on a small circuit board stiffener (**Figure 14**) mounted elsewhere in the PFP (instrument

462   interface board) to avoid the possibility of interference with sensitive analog circuitry. The MAVEN

463   magnetometer electronics were developed with many of the same electronics parts used for the Juno

464   instrument, which was built to operate in a more demanding radiation environment; as such, the

465   MAVEN instrument substantially exceeds the mission radiation requirement. The sensor assembly

466   is passive and radiation tolerant.

467

468   A common drive circuit in the analog electronics drives the two sensor ring cores into saturation at a

469   using a dedicated toroidal winding on each ring core. The ambient magnetic field in each sensor is

470   sensed by synchronous detection of the second harmonic of the drive frequency, the presence of

471   which reveals an imbalance in the response of the permeable ring core due to the presence of an

472   external field [*Acuña*, 2002]. As with any fluxgate, care must be taken to insure that the spacecraft

473   does not generate interference at harmonics of the drive frequency which could confuse the signal

474   attributed as an ambient magnetic field. The two magnetometers operate independently, and to

475   ensure that one does not interfere with the other, they are driven at different frequencies derived

476   from the master clock. Flight model 1 (FM1) uses a drive frequency of 15.2 kHz, and flight model 2

477   (FM2) uses a drive frequency of 16.3 kHz. This results in ample separation of the second harmonic

478   frequencies (30.4 kHz for FM1, 32.5 kHz for FM2).

479

480   The appropriate instrument dynamic range is selected, automatically, by range control logic within

481   the field programmable gate array (FPGA), resulting in autonomous operation through the entire

482   dynamic range. All range and instrument control functions are implemented in hardware. The FGM

483   powers up in operational mode autonomously, sending telemetry packets to the spacecraft C&DH

484   immediately without need of further commands. A limited command set allows us to tailor the

485   science and engineering telemetry to available resources (via averaging and decimation of samples

486   or packets) and to uplink changes in the parameters that control various functions as desired.

487
488   Power and Thermal Interface
489
490   Each magnetometer sensor board receives power from the PFDPU. There are two magnetometer boards

491   in the MAVEN implementation and each board receives an independent power service from the PFDPU

492   in order to maintain hardware redundancy. The magnetometer electronics requires +/-13V from the

493   PFDPU service. The MAG electronics uses local linear regulators to produce the required internal

494   voltages for analog VREF (+11.4V), current source (-8.5V), sensor analog to digital converters (+5V

495   and -5V), and digital logic levels (+3.3V and +2.5V). There is no EMI filter on the MAG board for the

496   +/-13V power supplied to MAG; this function is provided by the PFDPU power service.

497

498   The two magnetometer AC heater circuits require separate +28V supplies (+24V to +36V) and operate

499   independently and autonomously from the sensor electronics. These power lines pass through the PFP

500   but are powered independently of the PFP so that the MAG sensors are supplied with operational and

501   survival thermal power regardless of the state of the PFP. Each AC heater circuit operates

502   autonomously when the nominal spacecraft bus unregulated power is applied and requires no commands

503   or external configuration. The heater pulse width modulator (PWM) starts to activate at approximately

504   +30C and continues to increase power as the measured temperature drops to approximately -15C, at

505   which point the heater is fully on. The maximum power dissipated in the 80Ω heater is dependent upon

506   the (unregulated) power supply voltage.

507

508   The heater circuitry resides on a daughterboard resident on the power supply circuit board in the

509   PFDPU; it is physically separated from the MAG sensor electronics. A simplified block diagram of the

510   heater circuit is shown (**Figure 15**). The AC heater contains a transformer-coupled input that receives

511   3.3V level logic pulses from the DPU at a frequency of 131 kHz and a duty cycle of approximately 50%.

512   This is used to synchronize the AC heater pulse width modulation (PWM) circuitry to the PFDPU clock.

513   In the event that AC heater circuit power is on and the DPU clock is not present, an on-board oscillator

514   set close to the sync frequency will operate the PWM circuit. When the PFDPU is active, the heater

515   excitation frequency is synchronized to the PFDPU clocks. This is done to minimize interference with

516   other sensors (principally the Langmuir probe) on the payload.

517

518   Each magnetometer heater circuit provides a transformer-coupled heater monitor as an analog output to

519   the spacecraft. This service is provided in order to gain visibility into heater operation at times when the

520   PFP (and MAG) is powered off. The voltage output of the heater monitor is proportional to the power

521   dissipated in the 80Ω sensor heater resistance, providing an indirect measurement of sensor temperature

522   that is available in spacecraft telemetry.

523

524

525

526   iii.   Digital Implementation

527

528   The MAG electronics requires only simple logic and does not require the capability and complexity

529   of a microprocessor or software; it utilizes a single, low-power Field Programmable Gate Array

530   (FPGA). The required logic is contained within a single radiation-hard Aeroflex UT6325 FPGA

531   with +3.3V I/O. This design closely follows the Juno implementation, for which a very robust,

532   radiation tolerant instrument was required. This FPGA provides an ample logic capability as well as

533   internal radiation-hard memory. Aeroflex UT54ACS14E Schmitt-trigger inverters are utilized for

534   signals that interface to the PDFPU.

535

536   MAG receives serial commands from the PFDPU digital control board (DCB) and returns telemetry

537   to the PFPDPU for further processing and/or transfer to the spacecraft command and data handling

538   (C&DH) processor. The MAG board receives an 8.388 MHz clock (HFCLK) from the PFDPU

539   (2^{23} = 8,388,608 Hz) which provides the global clock used by the FPGA. A derivative of this

540   frequency is output to the analog sensor readout portion of the circuitry and utilized for resonant

541   tuning of the magnetometer.

542

543   The 1.048 MHz CMD_CLK signal supplied by the DCB is used to shift in the CMD data from the

544   DCB. The shift register outputs are synchronized internally to the main FPGA MAG_OSC clock

545   prior to use by the MAG Command Processor logic. The MAG has several commands associated

546   with instrument operation but does not require commands at startup to function. MAG does,

547   however, require HFCLK and CMD_CLK to produce science telemetry in the nominal operating

548   mode. The CMD_CLK is resynchronized to the internal HFCLK prior to use by the telemetry

549   processor.

550

551   1.   Data Modes

552

553   Each MAG electronics board communicates independently with the PFDPU, immediately upon

554   application of power, and receipt of clock, without need for commands of any kind. The MAG

555   telemetry consists of a block of telemetry sent every second to the PFDPU for further processing

556   and/or transmission to the spacecraft. The MAG uses this single telemetry format to communicate

557   science and engineering data to the PFDPU. This telemetry format consists of header information

558 (synchronization pattern, frame counter, spacecraft time information, and MAG status) as well as a
559 block of science measurements (three components of the vector magnetic field in sensor coordinates
560 at 32 vector samples per second) and a block of analog and digital housekeeping information. Upon
561 receipt, and subject to ground command, the PFDPU selects a portion of this telemetry for
562 retransmission to the spacecraft and ground, tailoring the output to meet telemetry allocations and
563 science requirements.

564

565 The PFDPU may perform averaging and decimation of the native 32 vector samples/sec telemetry
566 to achieve a desired telemetry allocation. Thus sample rates of 32, 16, 8, 4, 2, 1 vector samples/sec
567 are available (independently) for each magnetometer. The PFDPU may also implement a simple 8-
568 bit differencing scheme that offers a factor of two data compression, exclusive of the uncompressed
569 header, for each instrument (independently). In our implementation, this data compression scheme
570 is lossless: if any of the differences exceed the 8-bit dynamic range allocated, the uncompressed
571 packet is transmitted instead. In both cruise and the Mars environment, this will occur (and indeed
572 has occurred) very infrequently. The difference mode may be selected by ground command, relayed
573 via the PFDPU; it has been used liberally throughout cruise to Mars.

574

575

576   2.   Range Change Algorithm

577

578 Each MAG electronics card provides logic for autonomous operation of the magnetometer sensor,
579 choosing an appropriate dynamic range (512, 2048, or 65,536 nT) depending on the environmental
580 field. Alternatively, the instrument dynamic range may be commanded (manual mode) via an
581 instruction passed to MAG via the PFDPU. Automatic range control is designed to work with
582 minimal mathematics operations (lacking a microprocessor) by simple inspection of the three
583 components of the measured magnetic field. The algorithm provides adequate hysteresis to prevent
584 multiple transitions ("toggling") in the vicinity of a threshold and uses a "look back" period to
585 prevent multiple transitions during spacecraft rolls; it is based on the Juno algorithm.

586

587 Each MAG allows a change of dynamic range only at a packet boundary (once per second). The
588 instrument range reported in the packet header thus represents the dynamic range of all samples

19

589   acquired in the corresponding one second interval. The MAG will range up (increasing dynamic

590   range, decreasing sensitivity) in order to prevent saturation of individual axes. The ranging

591   algorithm keeps track of how many times a measurement (in each component) exceeds a ranging

592   threshold (**Figure 16**); if this count exceeds a (programmable) threshold, the instrument will range

593   up at the next opportunity (packet boundary). This feature provides some noise immunity in that it

594   makes it unlikely that a spurious measurement, or a few spurious measurements, will inadvertently

595   trigger a range change.

596

597   Each MAG will range down (decreasing dynamic range, increasing sensitivity) to preserve as much

598   measurement resolution as possible. Ranging down works in a similar manner, but threshold

599   comparisons are made over a "look back" interval that is designed to encompass at least one spin

600   period. This is used to prevent undesired range changes that would otherwise occur when all three

601   components of the field drop below a threshold for only a portion of the spacecraft spin period. The

602   MAVEN spacecraft is not a spinning spacecraft, but it is required to perform rotations about

603   spacecraft principal axes from time to time to satisfy instrument calibration requirements.

604

605   The 512 nT dynamic range is anticipated to satisfy measurement requirements throughout the vast

606   majority of the mission, including the "deep dip" campaigns that bring the spacecraft to lower

607   altitudes. In this range, the 16 bit quantization provides more than adequate measurement resolution

608   (+/- 0.015 nT), and a greater dynamic range would be required only if the periapsis during one of

609   the deep dips occurred over a specific latitude and longitude corresponding to the most intensely

610   magnetized site in the Mars crust. This is unlikely to occur unintentionally but the instrument has

611   the capability to optimize the dynamic range should the very strongest field be encountered at

612   periapsis during a deep dip.

613

614

615   iv.   Radiation Environment and Parts Engineering

616

617   The MAVEN electronics parts radiation requirement is met by parts that are radiation tolerant to

618   TID 13 krads (Si) @ 100 mil Al. Additionally, electronic parts are required to meet a LET

619   threshold against latchup and SEE of 75 MeV-cm^2/mg (or undergo further testing). Additional

620   details are available in the MAVEN Environmental Requirements Document, MAVEN-SYS-
621   RQMT-0010. The MAVEN electronics design and implementation closely follows that of the Juno
622   magnetometer investigation [*Connerney et al.*, 2014], which was designed for a more severe
623   radiation environment (50 krads TID with a radiation design margin of 2). The MAVEN
624   magnetometers were built from the Juno parts list and as such greatly exceed the MAVEN radiation
625   requirement.

626

627   v.   Performance

628

629   Performance of the magnetometers was monitored throughout the test program (Table) using a
630   series of calibration procedures repeated before and after significant environmental tests. These
631   calibration procedures are discussed below and in more detail in *Connerney et al.*, [2014]. FM1
632   preceded FM2 through development and thus had a more extensive series of calibrations.

633
634   A sensor with linear response may be characterized by the sensor model:

635

636   $$[B] = [A] \begin{bmatrix} s_1\,(c_1 - o_1) \\ s_2\,(c_2 - o_2) \\ s_3\,(c_3 - o_3) \end{bmatrix}$$

637
638   Where the true field vector [B] may be expressed as a linear combination [A] of the sensor
639   response; here [A] is a nearly diagonal 3 by 3 matrix. The three components of the sensor response
640   in counts (c_i) are corrected for small offsets (o_i) and scaled to magnetic units with scale factors (s_i).
641   In practice we use near-unity s_i that are slight corrections to the nominal scale factors. The matrix A
642   is often called the "orthogonality matrix" and it is a function of the sensor construction and
643   alignment to the reference cube; it is used to express the measured field in the coordinate system
644   defined by the reference cube normal vectors. We compared calibrations performed prior to and
645   after vibration tests to demonstrate alignment stability to 0.03º or better. Similarly, across all
646   environmental tests, scale factors for both instruments varied by less than 4 x 10^{-4}.

647

648

649

650

21

651   Table 1: Schedule of calibration activities throughout the environmental testing program.

652

FM1	Thinshell	Zeros	MAGSAT
23Feb12		√	√
28Feb12	√	√	√
12Mar12	√	√	√
14Mar12	√	√	√
March 13-21 Thermal Balance			
18Apr12		√	√
April 21-23 Vibration			
19Apr12	√	√	√
25Apr12	√	√	√
27Apr12			
May 2-10 Thermal Cycles			
14May12	√	√	√
15May12		√	√
FM2			
13Mar12	√	√	
March 13-21 Thermal Balance			
21Mar12		√	√
20Apr12	√	√	√
April 21-23 Vibration			
25Apr12	√	√	√
30Apr12			
May 2-10 Thermal Cycles			
15May12	√	√	√

653
654
655   vi. Test Program

656

657   The MAVEN instruments followed the GSFC MAG group's standard laboratory setup and test

658   procedure. The sensor bobbins and sensor assembly are thermally cycled over a wide temperature

659   range for mechanical stress relief. The sensors are thermally cycled once from +75 ºC to -35 ºC

660   followed by 12 cycles from +60 ºC to -20 ºC. The magnetometer electronics progress through

661   resonant tuning of the analog input circuitry and frequency response verification, followed by

662   voltage, temperature, and frequency margin testing (VTFMT) in the lab. This involves

663   comprehensive functional testing at hot and cold temperature extremes (+80 ºC to -40 ºC) while

664   varying voltages and frequencies over their margined envelopes. The electronics and sensor were

665   also assayed for biological contamination prior to delivery.

666

667   The magnetometer electronics were integrated to the main electronics box of the PFP and

668   experienced environment tests as part of the PFP instrument suite including thermal vacuum,

669   thermal balance, the full array of electromagnetic compatibility tests, and vibration. Before and

670   after each test element, comprehensive end-to-end functional tests were performed to provide

671   system-level baselines for MAG. While it is not feasible to perform accurate magnetic calibrations

672   without access to the magnetic test site, functional performance and sensor noise levels were

673   established within two four-layer Mu-metal shield cans. These shielded enclosures were designed

674   to protect the sensors from physical damage throughout integration with the PFP at the University

675   of California, Berkeley, and later in the ATLO environment at Lockheed Martin's Waterton Canyon

676   facility in Denver. Each of the multilayer Mu-metal shielded enclosures was fitted with a computer-

677   controlled tri-axial coil system that was used inside the shield cans for both AC and DC stimuli.

678   This allowed full functional verification throughout integration and test at Lockheed's facility. The

679   magnetometer sensors were to be mounted, eventually, at the outer end of the solar panels, but

680   throughout much of ATLO the solar panels are not physically present. Therefore the sensors were

681   mounted atop the spacecraft buss, within their protective enclosures, to facilitate integration and test

682   while awaiting final assembly.

683

684   vii.   Calibration

685

686   Calibrations of the MAVEN MAG instruments were performed on numerous occasions at system and

687   subsystem levels. We used subsystem level calibrations on the FGMs to establish performance

688   characteristics well in advance of system level calibrations. Later in development, when the Flight

689   Models (FMs) were available, system level calibrations were performed before and after each element of

690   the environmental test program (e.g., vibration, thermal vacuum) to establish that exposure to extreme

691   environmental conditions did not alter the instrument response to magnetic fields. At the system level,

692   our reference coordinate system is determined by the non-magnetic reflective optical cube affixed to

693   each sensor. These small optical cubes (0.5 inch on a side) are fabricated to 10 arcsec orthogonality and

694   all cubes were independently measured by the optics branch at GSFC. The magnetometer response is

695   determined relative to this cube. Calibrations relative to the optical cube include both intrinsic sensor

696   performance and the stability of the mechanical system that serves to bind all elements to each other.

697

698   Magnetic calibrations were performed at the GSFC Mario H. Acuña (MHA) Magnetic Test Facility

699   (MTF), a remote facility located adjacent to the GSFC campus. The MTF includes a 22 foot diameter

700   Braunbeck coil system (building 303), and associated control (building 304) and reference (building

701   309) structures, as well as other facilities. The 22 foot facility is sufficient to calibrate magnetometers to

702   better than 100 parts per million (ppm) absolute accuracy for applied fields in all directions and field

703   magnitudes up to about 1 Gauss. An independent measurement of applied magnetic fields is provided by

704   Overhausen Proton Precession magnetometers (reference magnetometer) placed near the unit under test.

705   The Proton Precession magnetometers provide an absolute measurement of the applied field over the

706   dynamic range of about 20,000 nT to 1.2 Gauss (120,000 nT). The facility is operated in a closed loop

707   with a remote reference vector magnetometer to null variations in the earth's field so applied fields may

708   be held constant to a fraction of a nT over the duration of a calibration sequence.

709

710   Two independent methods were used to calibrate the MAVEN magnetometers. The vector fluxgates are

711   calibrated in the 22' facility using a method ("MAGSAT method") developed by Mario Acuña for

712   calibration of the magnetometer flown on the MAGSAT mission. This technique uses precise 90 degree

713   rotations of the sensing element and a sequence of applied (facility) fields to simultaneously determine

714   the parameters of the magnetometer model response as well as a similar set of parameters that describe

715   the facility coil orthogonality [*Acuña,* 1981; a more accessible reference is *Connerney et al.,* 2014]. The

716   method takes advantage of the accuracy with which the orientation of the sensor (reference optical cube)

717   may be determined via autocollimation with a set of precision theodolites or alternately laser

718   autocollimators. We used a pair of T-3000 theodolites permanently affixed to the coil facility structural

719   members for this purpose. The method uses a sequence of applied fields of known magnitude aligned

720   with the coil system symmetry axes (north-south, east-west, up-down) with the sensor oriented in a

721   minimum of 3 orientations, as determined above, representing precise 90 degree rotations from the

722 initial orientation. All of the elements of the linear sensor response may be determined by inverting the

723 resulting overdetermined linear system [*Connerney et al*, 2004].

724

725 The second calibration method, developed by the DTU researchers (called the "thin shell" method,

726 alternately the "Orsted" method) uses a large set of rotations in a known and stable field to obtain much

727 the same instrument parameters, subject to an arbitrary rotation [*Risbo et al.,* 2002]. This method can be

728 performed at a suitable (i.e., magnetically quiet) location using the earth's field as a reference, simply by

729 making a sufficient number of measurements of the vector field measured by the sensor in many

730 orientations relative to the ambient field – thus the name: "thin shell". This method also employs a

731 Proton Precession reference magnetometer to measure the ambient field magnitude and account for any

732 variations in the field during the test. Of course, this method can also be employed in a magnetic test

733 facility at any desired field magnitude within the dynamic range of the facility. So we have also

734 performed calibrations of the MAVEN magnetometers in our facility at several applied field magnitudes

735 (which we call "thick shell" or nested thin shell calibrations) using this method; these may be performed

736 relatively quickly.

737

738 The "thin shell" method by itself determines the magnetometer sensor response in an unknown

739 coordinate system – an "intrinsic" coordinate system of the magnetometer sensor – the orientation of

740 which needs to be determined by other means. This is equivalent to stating that the parameters of the

741 linear sensor model may be determined subject to an arbitrary rotation, or, that only the symmetric part

742 of the sensor response matrix is established via a "thin shell" calibration.

743

744 Sensor zero offsets are determined in the magnetic facility by physically reversing the sensor in a weak

745 field, or by rotating the sensor in a weak (or zero) field. This may be done either in the center of the coil

746 system, operated in nulling mode, or inside of a suitably demagnetized, multi-layer mu metal shield can.

747
748
749
750
751
752   b. In-Flight Calibrations

753

754 In-flight calibrations are designed to monitor stability of magnetometer offsets and to provide a
755 capability to diagnose and monitor spacecraft-generated magnetic fields. In most applications, the
756 magnetic sensors are fixed in the spacecraft reference frame, and a constant magnetic field in the
757 sensor (sensor offset or bias) is indistinguishable from a constant ("static") spacecraft-generated
758 magnetic field. Thus it is common practice to lump them together and estimate the sum of the
759 sensor offset and static spacecraft magnetic field. This may be done by performing spacecraft
760 rotations in the environmental magnetic field.

761

762   i. Fluxgate Zeros and Static Spacecraft Field Determination

763

764 The mission plan allows for magnetic calibration maneuvers (roll maneuvers) that are scheduled to
765 occur during the science collection phase approximately every other month, interleaved loosely with
766 calibration maneuvers scheduled for the UVS investigation on a similar cadence. Two MAG
767 calibration roll activities have already been conducted during cruise operations. Another set of
768 MAG calibration maneuvers is scheduled to occur during transition orbit phase, and subsequent
769 maneuvers will be scheduled throughout science phase. Care is taken to schedule the MAG
770 calibration maneuvers to occur when (where) the spacecraft is more likely to experience a relatively
771 benign environment – i.e., times and places where the magnetic field is more likely to be relatively
772 quiet and not large in magnitude. For example, MAG calibrations will avoid periapsis where large
773 variations in the magnetic field are expected and regions of near Mars space characterized by large
774 field fluctuations (e.g., magnetosheath).

775

776 The periodic MAG calibration sequences (MAGROLLS) are designed to provide ~12 rotations
777 about one axis, followed immediately by another ~12 rotations about a second sc axis. These
778 execute at ~2 degrees per second rotation rate and each set of 12 rotations require about 42 minutes
779 to complete. Prior to execution of the maneuver, a command is sent to reduce the spacecraft battery
780 state of charge (SOC) to 80%, which effectively shuts off the solar arrays for the duration of the
781 maneuver. This is done to eliminate the possibility of variable fields associated with solar array
782 circuitry that might arise under variations of solar illumination angle (the subject of another set of
783 in-flight tests). **Figure 17** shows the magnetic field measured during MAVEN's second
784 MAGROLL sequence performed on day 183, 2014. A set of rotations about two different axes is

785   sufficient to uniquely determine the combined sensor offsets/spacecraft field as long as the

786   spacecraft magnetic field does not vary during the maneuvers. The rolls occur about the spacecraft

787   principal moments of inertia, which depend on deployments, and are not aligned with the spacecraft

788   payload coordinate system. For simplicity we refer to the roll axis closest to the spacecraft z axis as

789   the "z axis" roll, and that closest to the x axis as the "x axis" roll. Inspection of the vector field

790   during these rolls demonstrates that the rotation axes are not closely aligned with the spacecraft

791   payload axes in the cruise (stowed) configuration.

792

793   We will use the term "offset" to describe the combined sensor zeros and spacecraft static field in

794   what follows. We use a statistical least-squares estimation algorithm described by *Acuña* [2002] to

795   estimate offsets. This method was developed to estimate offsets using the Alfvenic properties of the

796   solar wind, that is, the observation that magnetic field variations in the solar wind tend to be

797   variations in angular direction, preserving the magnitude of the field. The method works very well

798   applied to spacecraft rolls where the variations in the vector field ought to preserve the field

799   magnitude as well. The offset vector ($\boldsymbol{O}$) is obtained from a series of vector measurements (i =

800   1,2,3,…n) of the magnetic field,

801

802    $\boldsymbol{O} = \left[\, 0.5 \left(\boldsymbol{B}_i + \boldsymbol{B}_{(i+l)}\right) \Delta \boldsymbol{B}_i \,\right] \left[\, \Delta \boldsymbol{B}_i \,\right]^{-1}$

803

804   Where the difference $\Delta \boldsymbol{B}_i = \boldsymbol{B}_i - \boldsymbol{B}_{(i+l)}$ may be formed using sequential measurements of the

805   vector field ($l = 1$) or measurements separated by l samples, chosen to provide a suitable vector

806   difference $\Delta \boldsymbol{B}_i$, compared to measurement noise or instrument quantization step size, but not so

807   large that variations in the field magnitude over l samples arise often. Applied to spacecraft rolls, l

808   should be chosen to provide difference point pairs over a small fraction of a roll period. The inverse

809   of the 3 x n matrix $\left[\, \Delta \boldsymbol{B}_i \,\right]$ is obtained using the singular value decomposition method [*Lanczos*,

810   1961]. Mario Acuña obtained the result above simply by observing that differences in the measured

811   vector field during a pure rotation of the field ought to be orthogonal to the ambient field, which is

812   simply the measured field minus the offset. *Leinweber et. al.* [2008] showed that this result may

813   also be obtained by assuming that variations in the field magnitude are uncorrelated with the

814   variance in differences of the three components. Simply stated, if the offsets are properly estimated,

815   the measured field magnitude will not evidence a spin modulation as the spacecraft rotates [see also

816   *Auster et al.,* 2002]. **Figure 18** shows the result of the offset estimation methodology applied to the

817 second MAGROLL maneuver obtained in cruise, which provides an estimate of the offset
818 appropriate to that time (and the state of the spacecraft at that time). The MAVEN spacecraft will
819 execute these maneuvers periodically, approximately every other month, as conditions dictate to
820 monitor stability of the offsets over time. The current plan calls for these observations to be
821 obtained in relatively low noise environments (solar wind, magnetotail), access to which is dictated
822 by the orbital evolution and to some extent solar wind conditions. The latter are unpredictable on a
823 time scale relevant to mission operations planning.

824

825 ii. Spacecraft-generated Magnetic Fields

826

827 Operation of the science instruments during cruise to Mars provided an opportunity to acquire
828 instrument and subsystem calibration and performance data, exercise operations processes that will
829 be required on orbit, and gain experience operating the instruments and the spacecraft. Operation of
830 the magnetometers during the cruise phase also provides the first magnetic measurements of the
831 spacecraft and systems, fully integrated and functioning in flight configuration, and operating in a
832 low field environment. During cruise we noted spacecraft-generated magnetic fields of low
833 amplitude associated with a few subsystems, notably thrusters (used infrequently after orbit
834 insertion and orbital period reduction), reaction wheels, and the power subsystem (solar array
835 circuits). The latter two sources are capable of producing fields of ~1 nT at the sensor locations,
836 under some circumstances. The Project is actively investigating mitigation strategies to reduce or
837 eliminate these effects during routine science operations.

838

839 The magnetic fields associated with the four reaction wheel assemblies appear at the (variable)
840 frequency of operation of the individual wheels when their speed falls within the passband (0-16
841 Hz) of the magnetometers. The periodic signal from these sources is typically of low magnitude (0.1
842 – 0.2 nT) but has been observed to increase in magnitude at very low reaction wheel speeds. Project
843 is currently evaluating a proposal to bias the reaction wheel speeds to higher RPMs during science
844 operations to shift the interference above the magnetometers passband (or to as high a frequency as
845 is practical).

846

847   We also observed variations in magnetic field associated with solar array operation that we have

848   identified with switching of one or more circuits residing on the outer solar array panels. We

849   originally detected a step variation if the field at the –Y sensor location (~1 nT) and the +Y sensor

850   location (~0.5 nT) during early cruise that occurred when the solar arrays were essentially switched

851   off via a command to reduce the state of charge of the batteries. An additional in-flight test is

852   planned prior to the start of science operations that will excite individual circuits on the outer panels

853   so we can uniquely identify the source and correct the field, analytically, using spacecraft telemetry

854   that identifies changes in switch state.

855

856

857 VI)   Operations and Data Processing

858

859   a.   Science Orbits Operations

860

861   The magnetometers were powered again on shortly after the Mars Orbit Insertion (MOI) maneuver

862   and they are to remain on throughout the mission. Orbital operations then largely of managing the

863   instrument sample rate to conform to the instrument telemetry allocation and planning spacecraft

864   maneuvers designed to diagnose and track any changes in spacecraft magnetic field and/or

865   instrument offsets. In late cruise and during early science operations, both instruments are being

866   operated at the same sample rate to assist in this process.

867

868   Current plans call for the magnetometer to sample at the high (32 vectors/s) rate throughout

869   periapsis (altitude less than 500 km) and at lesser rates throughout the rest of the orbit, subject to the

870   (time-variable) telemetry allocation. Telemetry allocations change throughout the mission subject to

871   practical limitations, such as the Earth-Mars distance and the number and frequency of downlink

872   opportunities afforded the Mission. In addition, the PFDPU collects and stores magnetometer data

873   at the highest rate continuously, and holds this data, along with that from the particle instruments

874   and the Langmuir and Plasma Wave Investigation, in memory aboard the spacecraft. This data

875   ("burst mode") is available for downlink upon command, after an examination of the "survey" data

876   already downlinked. The concept allows the science team to decide how to allocate precious

877   telemetry resources (downlink at high time resolution the data that's most interesting)

878   retrospectively, after a brief examination of the time series data downlinked at a lesser rate earlier.

879   Eventually the on-board memory is written over, making room for new burst mode observations.

880

881

882   b.   Data Processing

883

884   Ground processing of magnetometer data is performed routinely at GSFC following downlink and

885   transmission to the Science Data Center (SDC) at the University of Colorado, Boulder. An

886   automated script at GSFC searches the database at the SDC for data files that have yet to be

887   downloaded, executing hourly. Files identified as such are pulled to the MAG operations computer

888   automatically and queued for immediate processing.

889

890   The MAG data processing is responsive to the need for rapid turn-around, since other instruments

891   require magnetic field vectors in their preliminary analysis, by design before spacecraft

892   supplementary engineering data is available for archive processing. A preliminary MAG data

893   processing pipeline (**Figure 19**) executes prior to receipt of reconstructed spacecraft ephemeris

894   (NAIF SPK kernels) and attitude information (NAIF C-kernels) necessary for archive processing,

895   and without benefit of engineering telemetry that may be necessary for detailed analysis.

896   Preliminary processing is conducted to assess the health and safety of the instrument, producing

897   time series magnetic field vectors in either sensor or spacecraft payload coordinates that are useful

898   in diagnosing instrument offsets and spacecraft-generated magnetic fields.

899

900   A similar but more comprehensive archive processing pipeline (**Figure 20**) incorporates

901   reconstructed spacecraft ephemeris and attitude information, and any supplementary spacecraft

902   engineering information, producing magnetic field vectors, and spacecraft position vectors, in a

903   variety of coordinate systems of interest.

904

905   Both processing pipelines utilize the same code which is designed to retain the ability to process

906   data when supplementary data is lacking for a complete analysis. The data flow is designed to be

907   extremely flexible in the ability to assimilate unanticipated observations, such as engineering

908   telemetry that may be desired for analysis, and not anticipated early in the mission. This facility is

909 implemented by utilizing a decommutated telemetry file that passes data to the main processing
910 program in a text "keyword = value" format, originally developed for the Mars Observer and Mars
911 Global Surveyor Projects.

912

913   i. Telemetry De-commutation

914

915 Raw binary MAG packets are checked for errors and decommutated using a bit map appropriate to
916 the instrument mode (sample rate, differencing scheme if elected). Each data packet contains
917 sufficient information within its header to allow processing of the data that it contains, from a
918 magnetometer only perspective (i.e., excluding any spacecraft engineering data that may be
919 required). The decom program produces a decommutated telemetry file (".dtl" extension) that is an
920 ASCII stream of "keyword = value" pairs, utilizing a text format similar to that employed by JPL's
921 NAIF text kernel readers.

922

923   ii. MAG Packet Processing

924

925 MAG packet processing operates on the dtl input files, converting instrument counts to magnetic
926 field in nanoteslas, and engineering measurements in counts to engineering units, using calibration
927 files for the instruments and conversion coefficients for engineering quantities (currents,
928 temperatures, voltages, etc.). A SCLK (spacecraft clock) conversion file, provided by NAIF, is
929 required to convert spacecraft clock words to Coordinated Universal Time (UTC), and a
930 leapseconds kernel file ("leap.ker"), also provided by NAIF, is required to maintain accuracy of
931 UTC time conversions. The input files may contain sensor data from either or both of the
932 magnetometers, depending on whether the two (independent) data streams are merged, and as is the
933 case in archive processing, may contain supplementary spacecraft engineering data (e.g., solar array
934 currents, solar array switch states, etc.) for use in spacecraft magnetic field mitigation.

935

936 Archive processing adds access to reconstructed spacecraft ephemeris (SPK) and attitude
937 information (C-kernels) that are delivered somewhat later than the instrument science data on a
938 schedule dictated by Project. The Project currently envisions a weekly delivery of bested C-kernels,
939 which are pieced together from a set of many smaller files that contain overlapping data in places,

940   abundant data gaps, and retransmission duplicates. The C-kernels are required to render spacecraft

941   position and magnetic field vectors in the desired coordinate systems. These vectors appear in

942   Cartesian coordinates on output records, one record per observation, at the highest time resolution

943   available, for science data archive. Archive processing may also include spacecraft supplementary

944   engineering data, merged with the instrument science data in dtl files, should that be necessary in

945   processing a correction for time-variable spacecraft-generated magnetic fields. Where necessary

946   engineering data is not available with the required time cadence, interpolation of the engineering

947   data may be required; if interpolation is not feasible, as an alternative, the magnetic field vectors

948   may be averaged and resampled, if necessary. Static spacecraft magnetic fields are compensated via

949   subtraction of a constant (for example, determined from a previous spacecraft roll maneuver, or

950   MAGROLL calibration sequence) that is passed to the analysis program via the input dtl file.

951

952   iii.   NAIF Kernel Utilities for Ancillary Engineering

953

954   The only component on the spacecraft that articulates is the Articulated Payload Platform (APP),

955   since the spacecraft solar arrays and the high gain antenna are all fixed. A moving component or

956   subsystem is a potential source of a variable spacecraft magnetic field, if it has a significant

957   magnetic moment. The APP will be calibrated after deployment (post-MOI) by taking observations

958   of celestial objects in different directions, and before science operations begin, an in-flight magnetic

959   compatibility test will be performed. This test consists of cycling the APP through rotations about

960   the two articulation axes while the magnetic sensors record the magnetic field. In the event that the

961   APP produces a variation in the magnetic field sensed by the magnetometers, an attitude kernel (C-

962   kernel) for the APP will be available for use by the team in applying a correction.

963

964   iv.   Spacecraft Magnetic Field Mitigation

965

966   A static spacecraft magnetic field or instrument offset is measured via periodic spacecraft roll

967   maneuvers and eliminated in data processing either via adjustment of sensor zeros in the instrument

968   calibration file or by insertion of an offset variable in the decommutated telemetry file for each

969   sensor. As of this writing we anticipate that a dynamic correction will be implemented to

970   compensate for the field produced by the solar array, using spacecraft telemetry on switch states and

971 measurements of the current produced by illumination of the arrays. Implementation of this
972 correction will follow analysis of the in-flight tests planned for execution in the near future. The
973 engineering telemetry necessary for this correction will be passed to the processing program via
974 augmentation of the dtl file. We also anticipate archiving the reaction wheel speeds along with the
975 magnetometer data to avoid confusion with environmental phenomena.

976

977   c. Standard Data Products

978

979 For immediate use by the science team, and other instrument teams, we provide a quicklook product
980 that consists of time-ordered records of magnetic field vectors in nanoteslas, rendered in spacecraft
981 payload coordinates, along with browse products that are useful in identification of intervals of
982 special interest. These files contain magnetic field processed with a static spacecraft field
983 approximation, but do incorporate the full sensor zeros, calibration scale factors, and sensor
984 orthogonality matrix conversion. These quicklook products are intended for preliminary analysis
985 and planning purposes and are not intended for science archive.

986

987 Archive products are produced in a variety of coordinate systems when final reconstructed
988 spacecraft ephemeris and attitude information is available. These include a planet-centered ("pc")
989 coordinate system, rotating with Mars (z aligned with the spin axis) and with the x axis through the
990 Mars IAU prime meridian; and a sun-state ("ss") coordinate system wherein the primary reference
991 vector (x axis) points from the object (Mars) to the sun and the secondary reference vector (y axis)
992 is in the Mars orbit plane (approximately opposite to orbital motion) such that the z axis is
993 northward. Both of these coordinate systems are also available with respect to any other body
994 ("object") of interest, for example, the satellites Phobos and Deimos.

995

996 Science archive products are pushed to the SDC on a regular schedule.

997

998 VII)   Summary
999

1000 The MAVEN magnetic fields investigation will provide accurate vector magnetic field observations
1001 throughout all phases of the mission at sample rates of up to 32 vector samples/s, depending on
1002 telemetry allocation. The instrumentation provides two-sensor vector measurements for spacecraft

1003 magnetic field mitigation and complete hardware redundancy for risk mitigation. Magnetic field vectors

1004 are provided in-flight for use by other payloads in optimizing data collection and telemetry utilization.

1005 Spacecraft maneuvers (MAGROLLS) will be performed during science operations approximately every

1006 two months to monitor spacecraft fields and sensor offsets, and a series of additional in-flight tests have

1007 been performed to diagnose and correct for small-amplitude spacecraft-generated magnetic fields. These

1008 data, together with the synergistic particle observations acquired by the PFP instrumentation, and

1009 observations of plasma waves, ultraviolet emissions, and mass spectrometry, will form the foundation of

1010 a comprehensive study of the Mars atmosphere and its evolution.

1011

1012   References

1013

1014   Acuña, M. H., (1981). MAGSAT – vector magnetometer absolute sensor alignment determination.
1015   NASA Technical Memorandum, 79648.

1016   Acuña, M. H., (2002). Space-based magnetometers. *Review of Scientific Instruments* **73**, No. 11, 3717-
1017   3736.

1018   Acuña, M. H., Connerney, J. E. P., Wasilewski, P., et al. (1998). Magnetic field and plasma observations
1019   at Mars: Initial results of the Mars Global Surveyor Mission, *Science,* **279***,* 1676-1680.

1020   Acuña, M. H., Connerney, J. E. P., Ness, N. F., et al. (1999). Global distribution of crustal magnetism
1021   discovered by the Mars Global Surveyor MAG/ER Experiment. *Science* **284**: 790-793.

1022   Acuña, M. H., Connerney, J. E. P., Wasilewski, P., *et al.* (2001). The magnetic field of Mars: Summary
1023   of results from the aerobraking and mapping orbits. *Journal of Geophysical Research* **106**: 23403-
1024   23417.

1025   Andersson, L. A., R.E. Ergun, G.T. Delory, A. Erickson, The Langmuir probe instrument on MAVEN.
1026   *Space Sci. Rev.* (2014, this issue).

1027   Andersson, L., et al. (2010). The Combined Atmospheric Photochemistry and Ion Tracing code:
1028   Reproducing the Viking Lander results and initial outflow results. *Icarus* **206**(1): 120-129.Auster, H.
1029   U., fornacon, K. H., Georgescu, E., Glassmeier, K. H., and Motschumann, U. (2002). Calibration of
1030   fluxgate magnetometers using relative motion, *Meas. Sci. Technol.* **13**, 1124-1131.

1031   Barabash S., Fedorov A., Lundin R., Sauvaud J. A. (2007), Martian atmospheric erosion rates, *Science*
1032   **315**(5811): 501-503.

1033   Bertaux, J. –L., F. Leblanc, O. Witasse, E. Quemerais, J. Lilensten, S.A. Stern, B. Sandel, O. Korablev,
1034   (2005) Nature **435**, 790-794. doi:10.1038/nature03603.

1035   Bertucci, C., Mazelle, C., Crider, D. H., Vignes, D., Acuña, M. H., Mitchell, D. L., Lin, R. P.,
1036   Connerney, J. E. P., Reme, H., Cloutier, P. A., Ness, N. F., Winterhalter, D. (2003), Magnetic field
1037   draping enhancement at the Martian magnetic pileup boundary from Mars global surveyor
1038   observations, *Geophys. Res. Lett.* **30**(2).

1039   Brain, D. A., Space Sci. Rev. **126**, 77-112 (2006).Brain, D. A., J. S. Halekas, L. M. Peticolas, R. P. Lin,
1040   J. G. Luhmann, D. L. Mitchell, G. T. Delory, S. W. Bougher, M. H. Acuña, and H. Rème (2006), On
1041   the origin of aurorae on Mars, *Geophys. Res. Lett.*, 33, L01201, doi:10.1029/2005GL024782.

1042 Brain, D.A., A. H. Baker, J. Briggs, J. P. Eastwood, J. S. Halekas, and T.‑D. Phan (2010), Episodic

1043   detachment of Martian crustal magnetic fields leading to bulk atmospheric plasma escape, *Geophys.*

1044   *Res. Lett.*, **37**, L14108, doi:10.1029/2010GL043916.

1045 Brain, D. A., and J.S. Halekas, in *Auroral Phenomenology and Magnetospheric Processes: Earth and*

1046   *Other Planets*, ed. by A. Keiling, E. Donovan, F. Bagenal, T. Karlsson (American Geophysical Union,

1047   Washington, D.C., 2012) pp.123-132. doi:10.1029/2011GM001201.

1048 Brain, D. A., in *Atmosphere and Climate of Mars*, eds. R. Haberle, T. Clancy, F. Forget, M. Smith, R.

1049   Zurek (Cambridge University Press, 2014), in press.

1050 Breuer, D. and T. Spohn, Early plate tectonics vs. single plate tectonics on Mars: Evidence from

1051   magnetic field history and crust evolution, *J. Geophys. Res.*, submitted, 2003.

1052 Connerney, J. E. P., Acuña, M. H., Wasilewski, P. J., Ness, N. F., *et al.,* (1999). Magnetic lineations in

1053   the ancient crust of Mars, *Science* **284**: 794-798.

1054 Connerney, J. E. P., Acuña, M. H., Ness, N. F., Spohn, T., and Schubert, G. (2004). Mars crustal

1055   magnetism. *Space Science Reviews* **111**(1-2): 1-32.

1056 Connerney, J. E. P., Acuña, M. H., Ness, N. F., Kletetschka, G. *et al.,* (2005). Tectonic implications of

1057   Mars crustal magnetism. *Proceedings of the National Academy of Sciences* **102**(42): 14970-14975.

1058 Connerney, J. E. P., et al., (2014). The Juno Magnetic Field Investigation. *Space Science Reviews*, in

1059   preparation.

1060 Dong, C.F., Bougher, S.W., Ma, Y.J., Toth, G., Nagy, A.F., and Najib, D., (2014) Solar wind

1061   interaction with Mars upper atmosphere: Results from the one-way coupling between the multi-fluid

1062   MHD model and the MTGCM model, Geophys. Res. Lett., doi:10.1002/2014GL059515.

1063 Ergun, R. E., Andersson, L., Peterson, W. K., Brain, D., Delory, G. T., Mitchell, D. L., Lin, R. P., Yau,

1064   A. W. (2006), Role of plasma waves in Mars' atmospheric loss, *Geophys. Res. Lett.* **33**(14).

1065 Espley, J.R., P.A. Cloutier, D.A. Brain, D.H. Crider, M.H. Acuña (2004), Observations of low-

1066   frequency magnetic oscillations in the Martian magnetosheath, magnetic pileup region, and tail, *J.*

1067   *Geophys. Res., 109*, A07213, doi:10.1029/2003JA010193.

1068 Glassmeier, K. H., and J. Espley (2006), ULF waves in planetary magnetospheres, *Magnetospheric ULF*

1069   *Waves: Synthesis and New Directions* **169**: 341-359.

1070 Halekas, J. S., Eastwood, J. P., Brain, D. A., Phan, T. D., Oieroset, M., Lin, R. P. (2009), In situ

1071   observations of reconnection Hall magnetic fields at Mars: Evidence for ion diffusion region

1072   encounters, *J. Geophys. Res.‑Space Physics* **114**.

1073 Jakosky, B. M., and R. J. Phillips (2001). Mars' volatile and climate history. *Nature* **412**(6843): 237-
1074   244.

1075 Jakosky, B., R.P. Lin, J. Grebowsky, J.G. Luhmann, D.L. Mitchell, D.A. Brain, R.J. Lillis et al., The
1076   2013 Mars Atmosphere and Volatile Evolution (MAVEN) mission to Mars. *Space Sci. Rev*. (2014,
1077   this issue).

1078 Lanczos, C. (1961) *Linear Differential Operations*, 564 pp., D. Van Nostrand, Princeton, N.J.

1079 Leinweber, H. K., Russell, C. T., Torkar, K., Zhang, T. L., and Angelopoulos, V. (2008). An advanced
1080   approach to finding magnetometer zero levels in the interplanetary magnetic field. *Meas. Sci. Technol.*
1081   **19**, 055104, doi:10.1088/0957-0233/19/5/055104.

1082 Lillis, R. J., Frey, H. V., Manga, M., *et al.* (2008) An improved crustal magnetic field map of Mars from
1083   electron reflectometry: Highland volcano magmatic history and the end of the martian dynamo. *Icarus*
1084   **194**: 575-596.

1085 Lillis, R. J., Robbins, S., Manga, M., Halekas, J. S. and Frey, H. V. (2013). Time history of the martian
1086   dynamo from crater magnetic field analysis. *Journal of Geophysical Research* **118**:1488-1511
1087   (doi:10.1002/jgre.20105).

1088 Luhmann, J. G., Russell, C. T., Brace, L. H., and Vaisberg, O. L., (1992) The intrinsic magnetic field
1089   and solar wind interaction with Mars, in *Mars,* eds. Hugh H. Kieffer, Bruce M. jakosky, Conway W.
1090   Snyder, and Mildred S. Matthews, University of Arizona press, 1090-1134.

1091 Lundin, R., et al., Space Sci. Rev. **126**, 333-354 (2006). doi:10.1007/s11214-006-9086-x.

1092 Ma, Y. J., Nagy, A. F., Sokolov, I. V., and Hansen, K. C., (2004) Three-dimensional, multi-species, high
1093   spatial resolution MHD studies of the solar wind interaction with Mars, *Journal of Geophysical*
1094   *Research* **109**, A07211, doi:10.1029/2003JA010367.

1095 Mahaffy, P. R., et al. (2013), Abundance and Isotopic Composition of Gases in the Martian Atmosphere
1096   from the Curiosity Rover, *Science* **341**(6143): 263-266.

1097 Mitchell, D., L., C. Mazelle, J.A. Sauvaud, D. Toublanc, Thocaven, Rouzaud, A. Federov, E.R. Taylor,
1098   M. Robinson, P. Turin, D.W. Curtis, The MAVEN Solar Wind Electron Analyzer (SWEA). *Space.*
1099   *Sci. Rev.* (2014, this issue).

1100 Nilsson, H., Edberg, N. J. T., Stenberg, G., Barabash, S., Holmstrom, M., Futaana, Y., Lundin, R.,
1101   Fedorov, A. (2011), Heavy ion escape from Mars, influence from solar wind conditions and crustal
1102   magnetic fields, *Icarus* **215**(2): 475-484.

1103 Nimmo, F. and Stevenson, D. (2000). Influence of early plate tectonics on the thermal evolution and
1104   magnetic field of Mars. *Journal of Geophysical Research* **105**: 11969-11976.

1105 Risbo, T., P. Brauer, J. M. G. Merayo, O. Nielsen, J. R. Petersen, F. Primdahl, and N. Olsen., (2002). Ørsted
1106   calibration mission: The thin shell method and the spherical harmonic analysis, in *Ground and In-Flight Space*
1107   *Magnetometer Calibration Techniques*, vol. ESA SP-490.

1108 Schubert G. and T. Spohn (1990) Thermal history of Mars and the sulfur content of its core, *J. Geophys.*
1109   *Res., 95*, 14,095-14,104.

1110 Schubert, G; S. C. Solomon, D. L. Turcotte, M. J. Drake, and N. Sleep (1992) Origin and thermal
1111   evolution of Mars, in *Mars*, ED: Kieffer, Hugh H; Jakosky, Bruce M; Snyder, Conway W; Matthews,
1112   Mildred S ,University of Arizona Press, Tucson, AZ, Pages 147-183.

1113 Sleep, N. H. (1994). Martian plate tectonics, *Journal of Geophysical Research* **99**: 5639-5655.

1114 Stevenson, D. J., T. Spohn, and G. Schubert (1983) Magnetism and Thermal Evolution of the Terrestrial
1115   Planets, *Icarus, 54*, 466-489.

1116 Yin, A. (2012) Structural analysis of the Valles Marineris fault zone: Possible evidence for large-scale
1117   strike-slip faulting on Mars. *Lithosphere* **4**: 286-330 (doi:10.1130/L192.1).

1118

1119
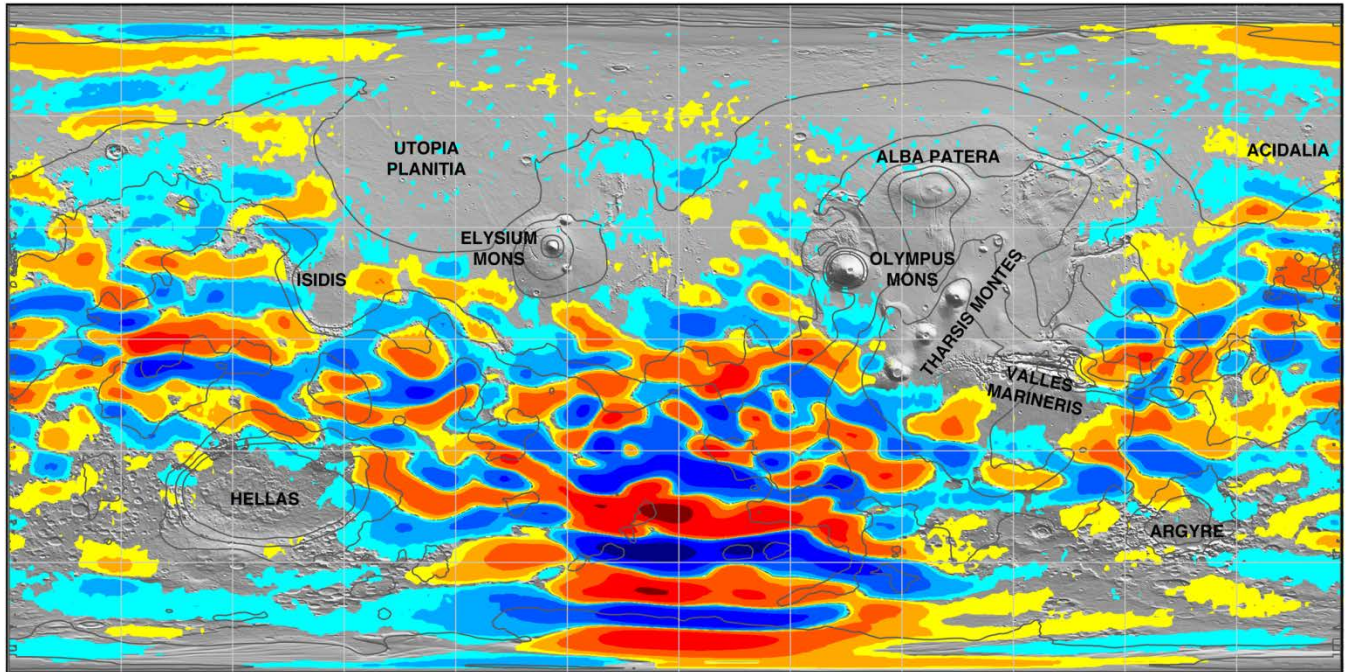
1120

1121 Figure 1: Map of the magnetic field of Mars observed by the Mars Global Surveyor satellite at a nominal
1122 400 km altitude (after *Connerney et al.,* 2005). Each pixel is colored according to the median value of
1123 the filtered radial magnetic field component observed within the 1º by 1º degree latitude/longitude range
1124 represented by the pixel. Colors are assigned in 12 steps spanning two orders of magnitude variation.
1125 Where the field falls below the minimum contour a shaded MOLA topography relief map provides
1126 context. Contours of constant elevation (-4, -2, 0, 2, 4 km elevation) are superimposed.

1127
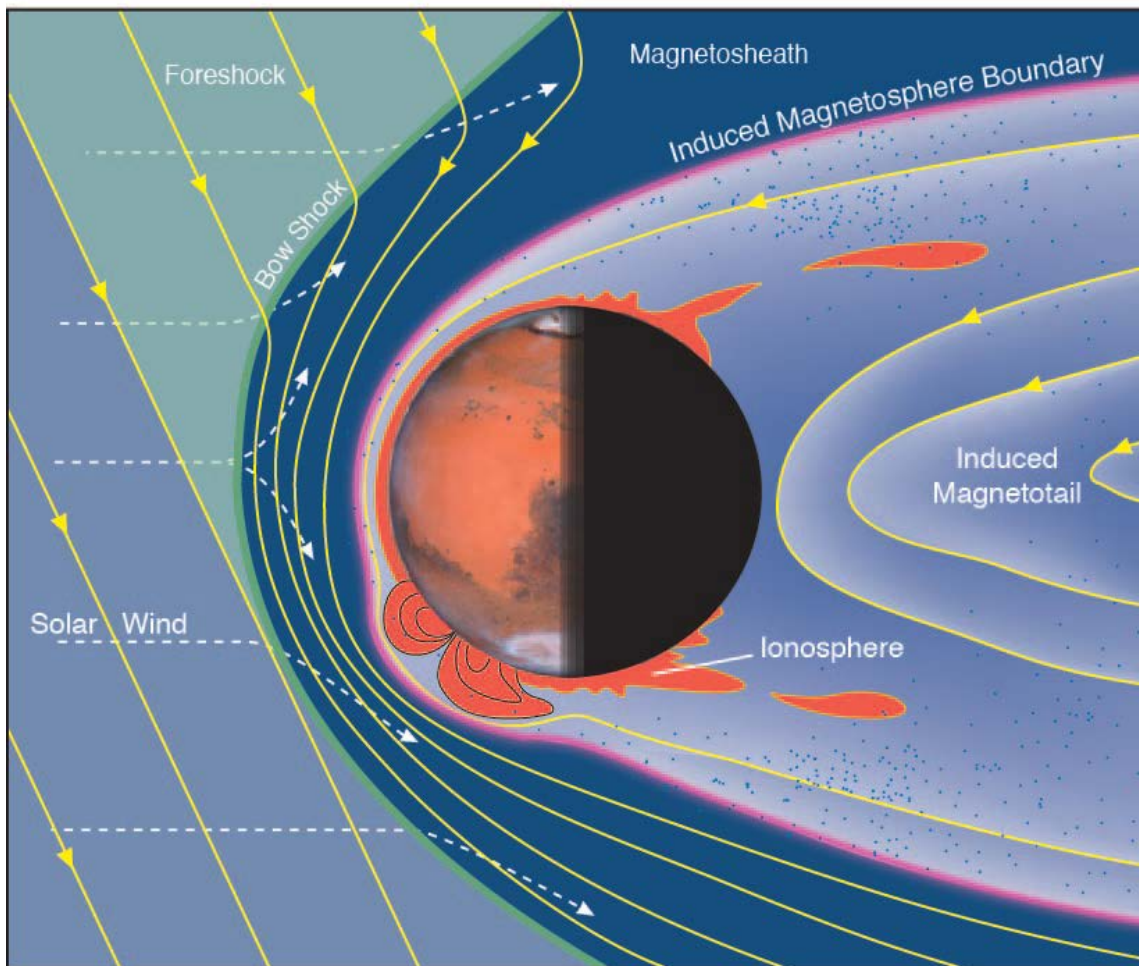
1128

1129 Figure 2: Schematic of the solar wind interaction with Mars (from *Brain et al.,* 2014). The solar wind

1130 carries with it the interplanetary magnetic field (yellow) as it streams (dashed lines) toward the bow

1131 shock (green) upstream of Mars. Intense crustal magnetic fields (orange) impose structure throughout

1132 localized regions of the upper atmosphere and ionosphere.

1133
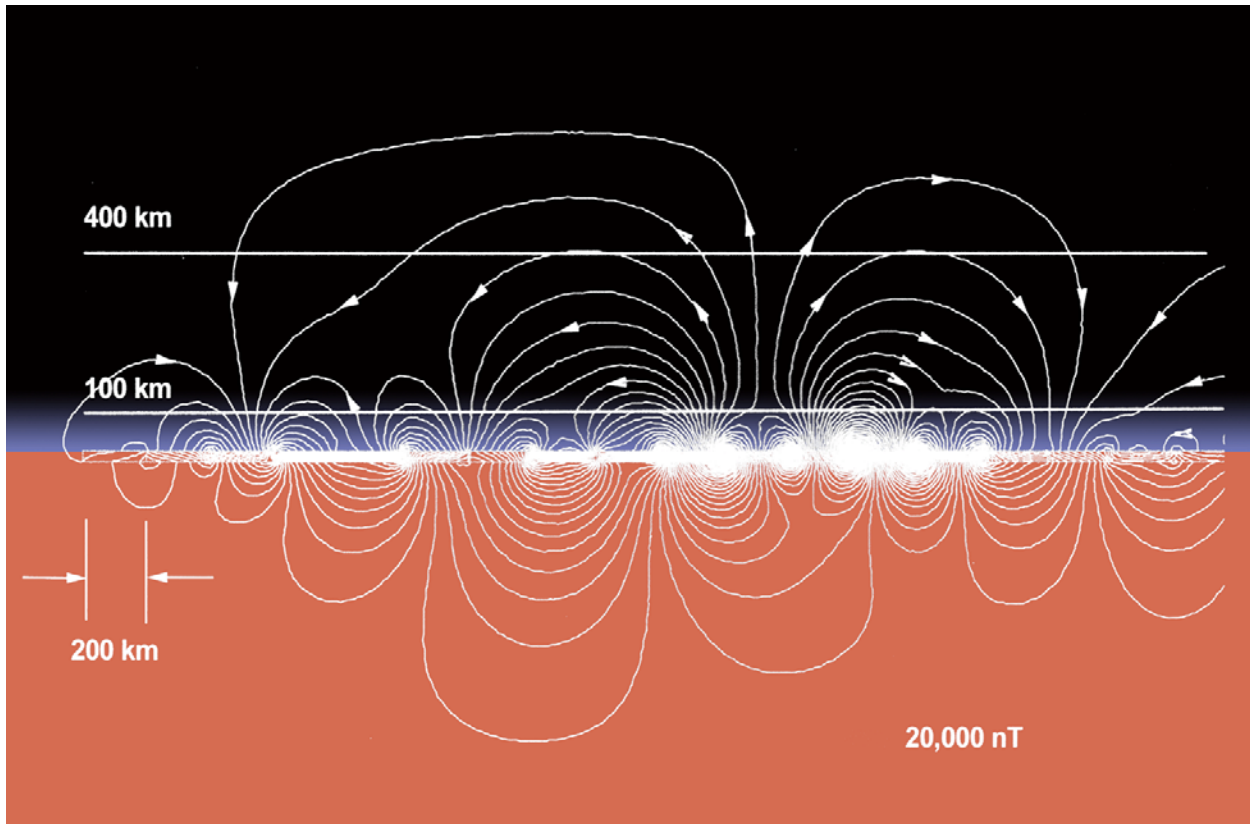
Figure 3: Plane projection of the magnetic field geometry above the intensely magnetized southern highlands based on the crustal magnetic field model of *Connerney et al.,* [1999]. This figure illustrates the field geometry that would be encountered during periapsis passes along a line of constant longitude (near 150 degrees east) and centered at 50 degrees south latitude. Similar "mini-magnetospheres" may be encountered above much of the magnetized crust, depending on spacecraft altitude and solar wind conditions.
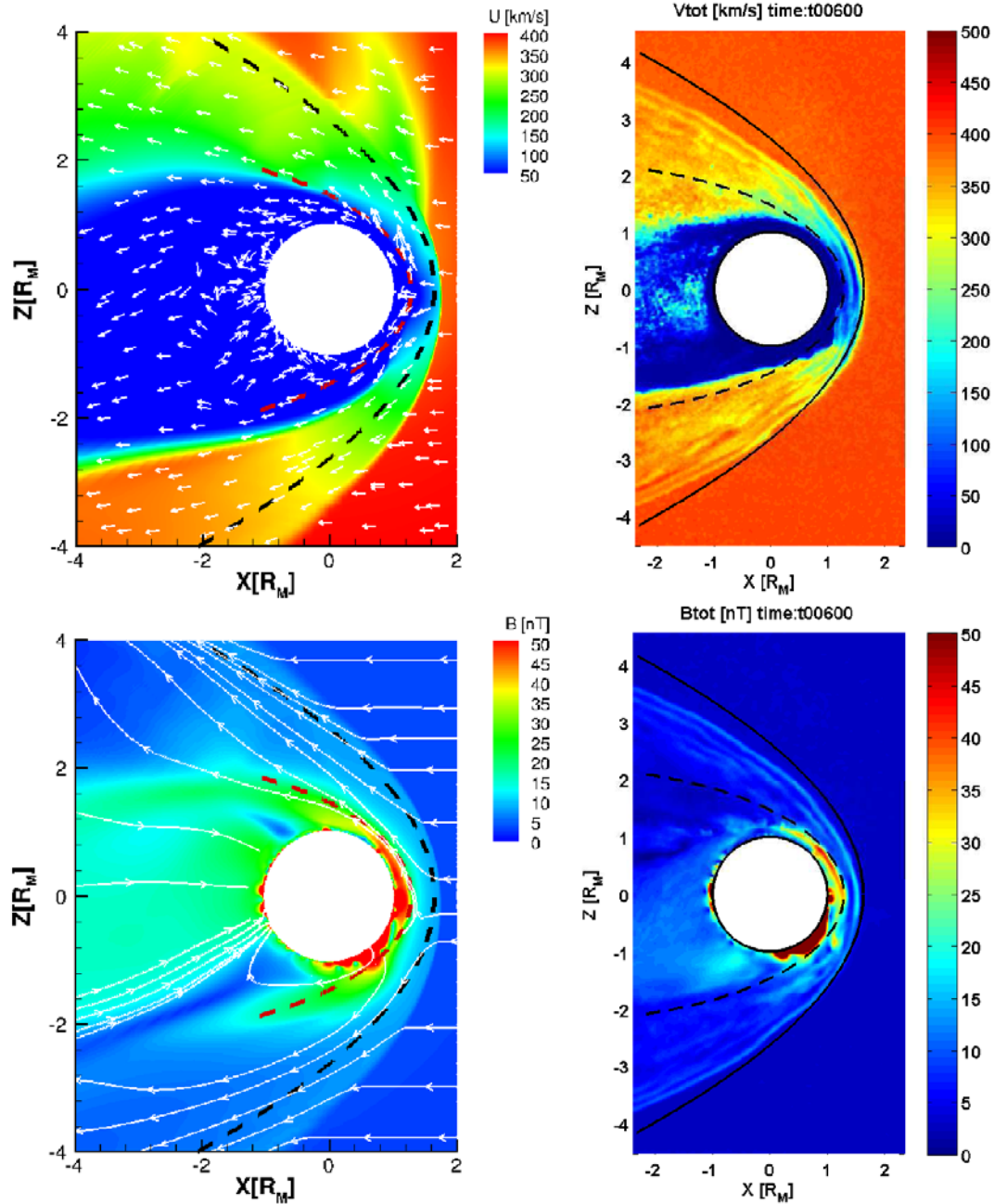
1143
1144
1145 Figure 4: Plasma and magnetic field environment of Mars according to the multi-fluid

1146 magnetohydrodynamic simulation of Dong and colleagues [*Dong et al.*, 2014]. Upper left panel is a

1147 meridian plane projection of the magnitude (color) and direction (arrows) of plasma velocity near Mars.

1148 Lower left panel shows the simulated magnetic field lines and magnetic field magnitude (colors) in

1149 meridian plane projection. Large field magnitudes very near the planet's surface are due to strong crustal

1150 magnetic fields, primarily in the southern hemisphere, but strong fields due to the solar wind interaction

1151 are also encountered at altitude on the day side of the planet.
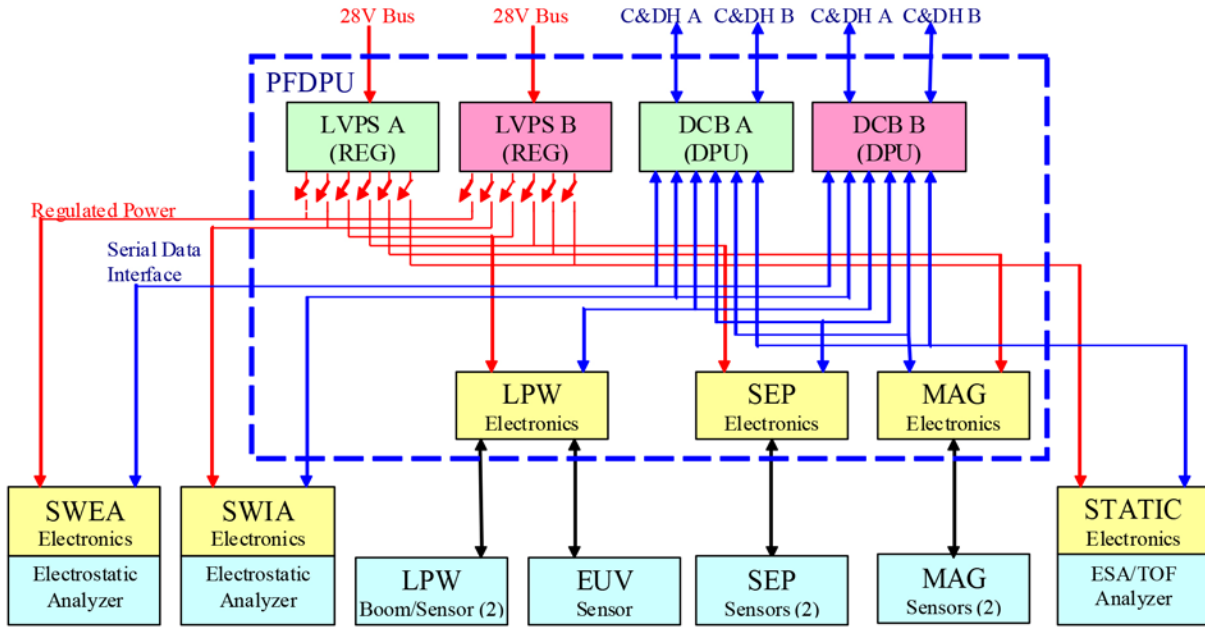
1152

1153

1154

1155   Figure 5: Schematic diagram of the Particles and Fields Package (PFP) and science instrumentation that

1156   it services. The PFP Digital Processor Unit (PFPDPU) consolidates instrument power service,

1157   command, and telemetry functions for the suite of instruments, presenting a single electrical interface to

1158   the spacecraft.
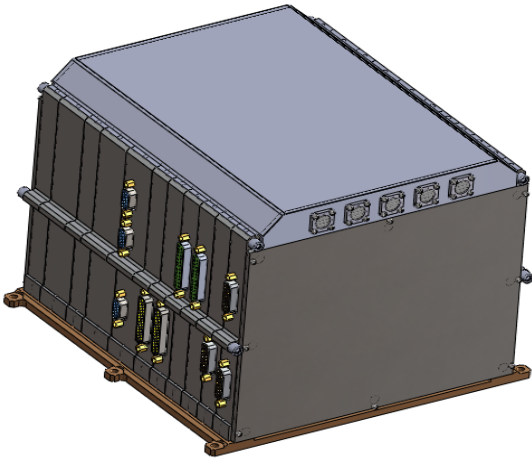
1159
1160
1161
Figure 6: The Particles and Fields electronics stack, accommodates electronics frames for each of the

instruments in the suite, in addition to redundant power supplies and command and data handling digital

processor units.

1165
1166

Figure 7: The MAVEN spacecraft in the clean room at Lockheed Martin during assembly. The (-Y)
MAG sensor (left extremity) is mounted at the end of the MAG "boomlet". A cautionary piece of yellow
tape hangs below the sensor. The sensor cover bears laminations of copper tape and Kapton tape
providing electrostatic and electromagnetic shielding.

1174

1175
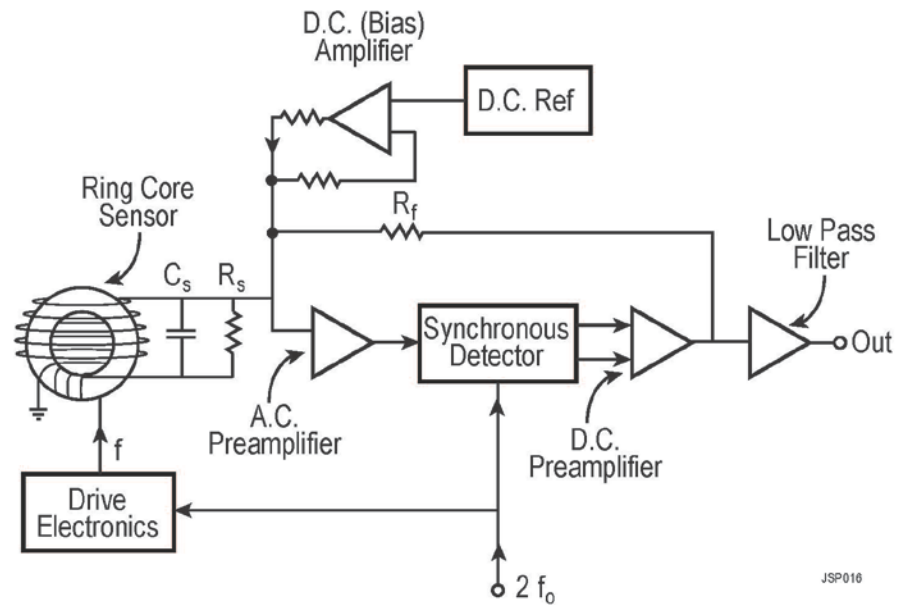
Figure 8: Schematic of a single-axis fluxgate magnetometer (after Acuña, 2002) utilizing a tuned ring-core sensor and a shared 2f sense and feedback coil.

1176
1177

1178
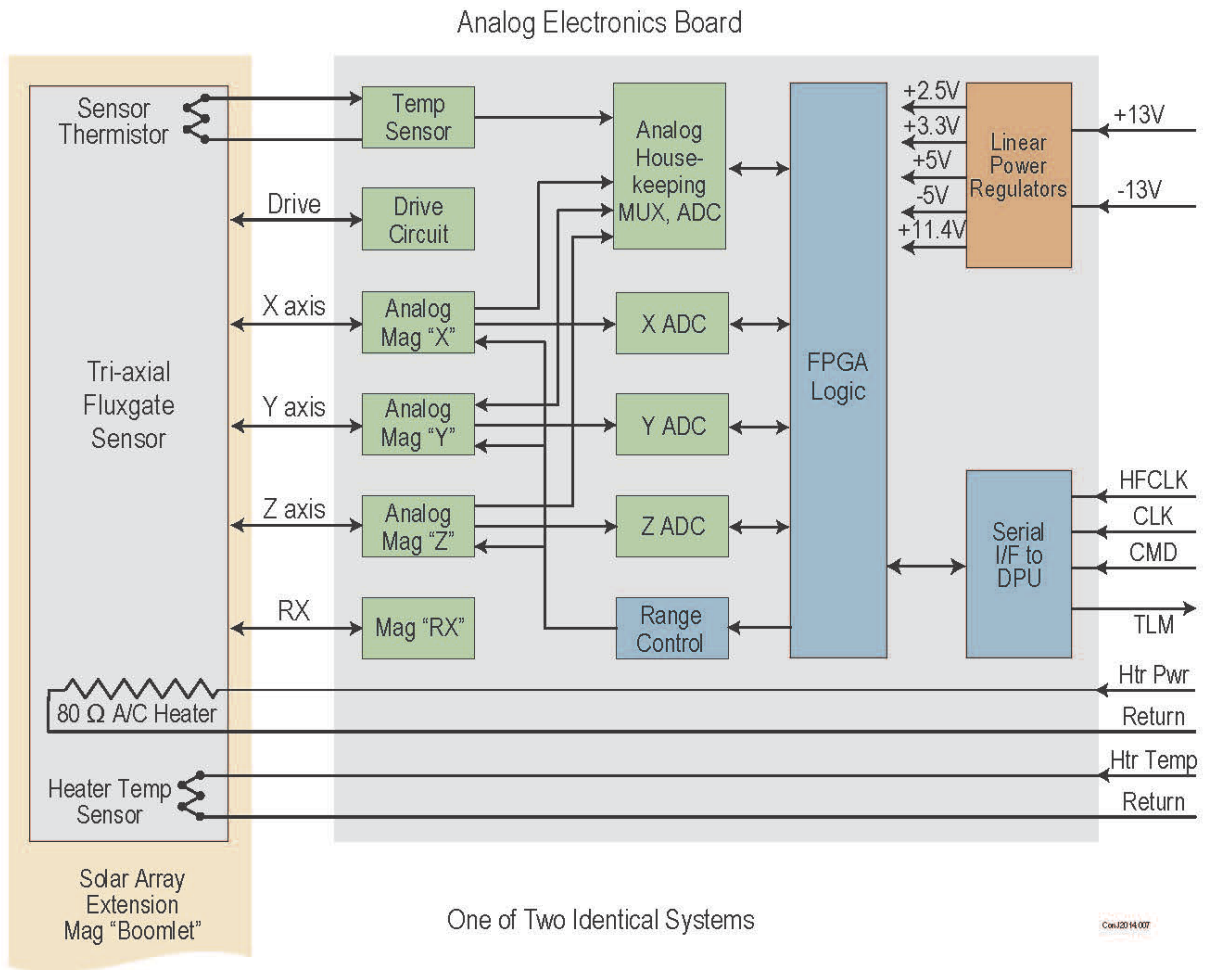
Figure 9: Simplified block diagram of one of the two identical MAVEN vector magnetometers. The tri-axial fluxgate sensor (left) is mounted on the MAG "boomlet" at the end of the solar array and harnessed to the electronics package mounted in the spacecraft body. The analog and digital electronics (right shaded portion) is contained on a single multilayer electronics board that is contained in a shielded enclosure (frame) within the PFP assembly.

1186

1187
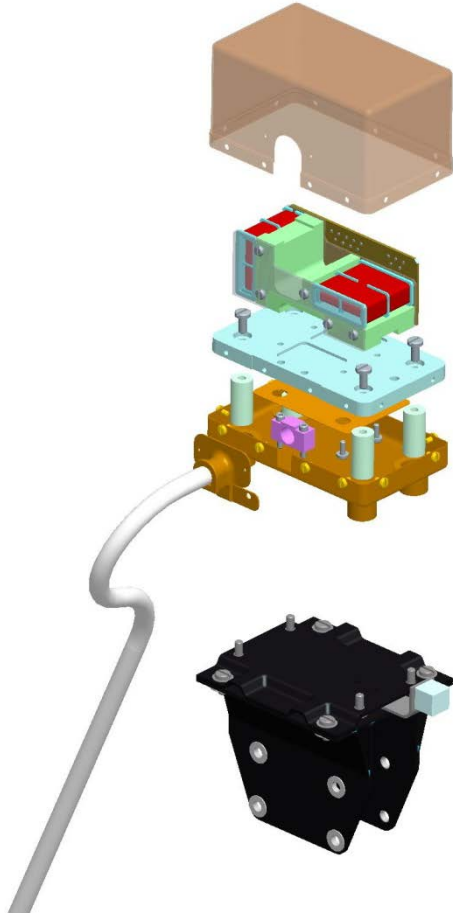
1188
1189

Figure 10: Expanded illustration of the sensor assembly showing the type LE phenolic sensor block

(green), nested sense and feedback coils (red), base (blue), thermal isolation feet (light blue), clam-shell

protective cover (tan), and carbon composite mounting bracket assembly (black) with attached

calibration cube.

1194

1195

1196
1197

1198
1199
1200

Figure 11: Photograph of the MAVEN magnetometer sensor assembly showing the phenolic sensor
block (brown), nested sense and feedback coils, and sensor printed circuit board. The sensor is provided
with a (shielded) pigtail connector to insure that interconnect hardware is kept at a sensible distance
from the sensor; nevertheless, all components installed on the MAG boomlets are subject to enhanced
magnetic screening prior to use.

1201
1202
1203
1204
1205
1206
1207

On-Demand Simp Rep2MAVEN_PAPER
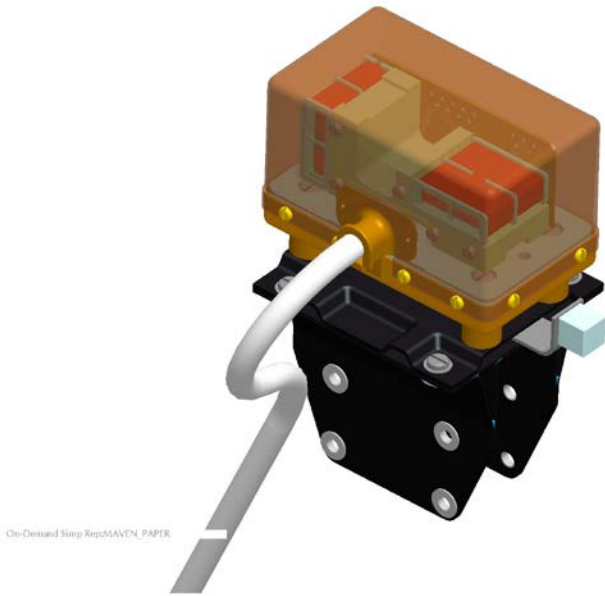
1208

1209

1210 Figure 12: Assembled sensor assembly. Once assembled, all parts of the sensor assembly remain

1211 assembled except for the lower part of the carbon composite mounting bracket assembly (black) that

1212 attaches to the MAG "boomlet". The top part of the mounting bracket with the attached optical cube

1213 remains in assembly with the sensor block throughout the entire test and calibration program.

Figure 13: Magnetometer analog and digital board (one of two identical assemblies) in its shielded frame, top cover removed for viewing. The analog portion is to the left, where the sensor cable connector J25 resides, and the digital portion is to the right. The FPGA is the large square device on the upper right.

1224
1225
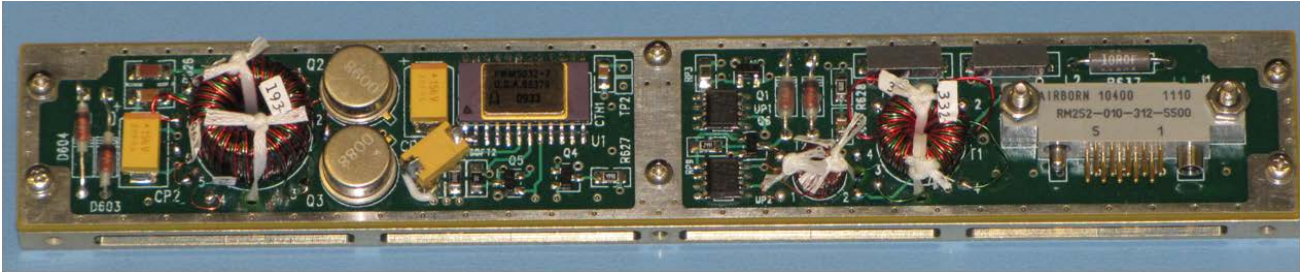
1226
1227
1228

1229 Figure 14: Magnetometer a/c heater board (one of two identical assemblies, mounted back-to-back) in

1230 its carrier frame. This assembly is mounted on the PFP instrument interface board.

1231

1232

1233

1234

1235

Sensor Thermistor

Sensor Heater (80 Ω)

Heater IMON

Heater Transformer

FGM Sensor

FET Driver

PWM Controller

Osc. Circuit — Sync / Return

Volt Reg

EMI Filter — +28V Htr / Return

Heater Current Monitor Return

Electronics Box

Conn.J2014.008
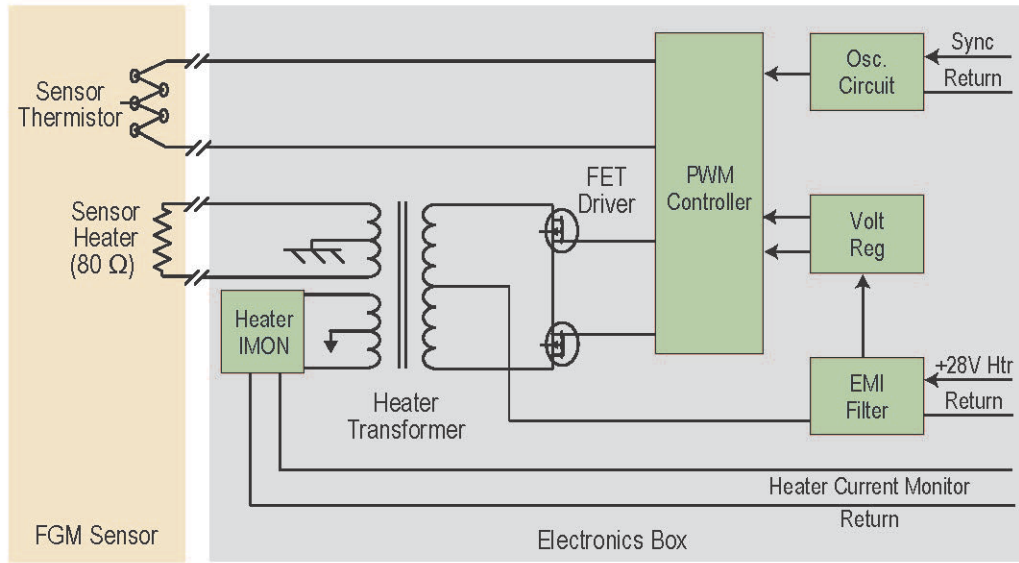
1236

1237

Figure 15: Simplified block diagram of one of the two identical MAVEN a/c heater electronics assemblies. The tri-axial fluxgate sensor (left) is mounted on the MAG "boomlet" at the end of the solar array. The heater control electronics (right shaded portion) is contained on a single multilayer electronics board that is integrated with the PFP instrument interface board (in order to minimize potential interference with sensitive analog electronics). A transformer-coupled heater monitor is made available to the spacecraft engineering telemetry so that the thermal power delivered to the MAG sensors may be monitored when the MAG electronics is powered off.

1245

1246
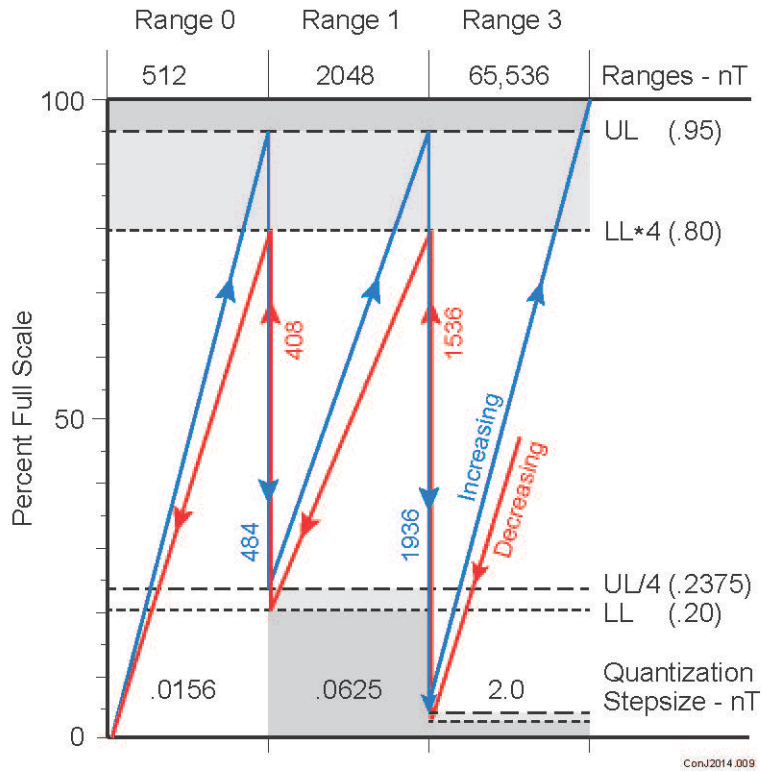
1247

1248

1249 Figure 16: Instrument autonomous range selection algorithm increases the instrument dynamic range to

1250 prevent saturation in response to an increasing (blue) magnetic field magnitude in any of the three vector

1251 components and decreases instrument dynamic range in response to a decreasing field (red). The

1252 algorithm uses "guard bands" to prevent rapid back and forth changes in dynamic range ("toggling") in

1253 the presence of field fluctuations near range limits. Nominal threshold values are shown.
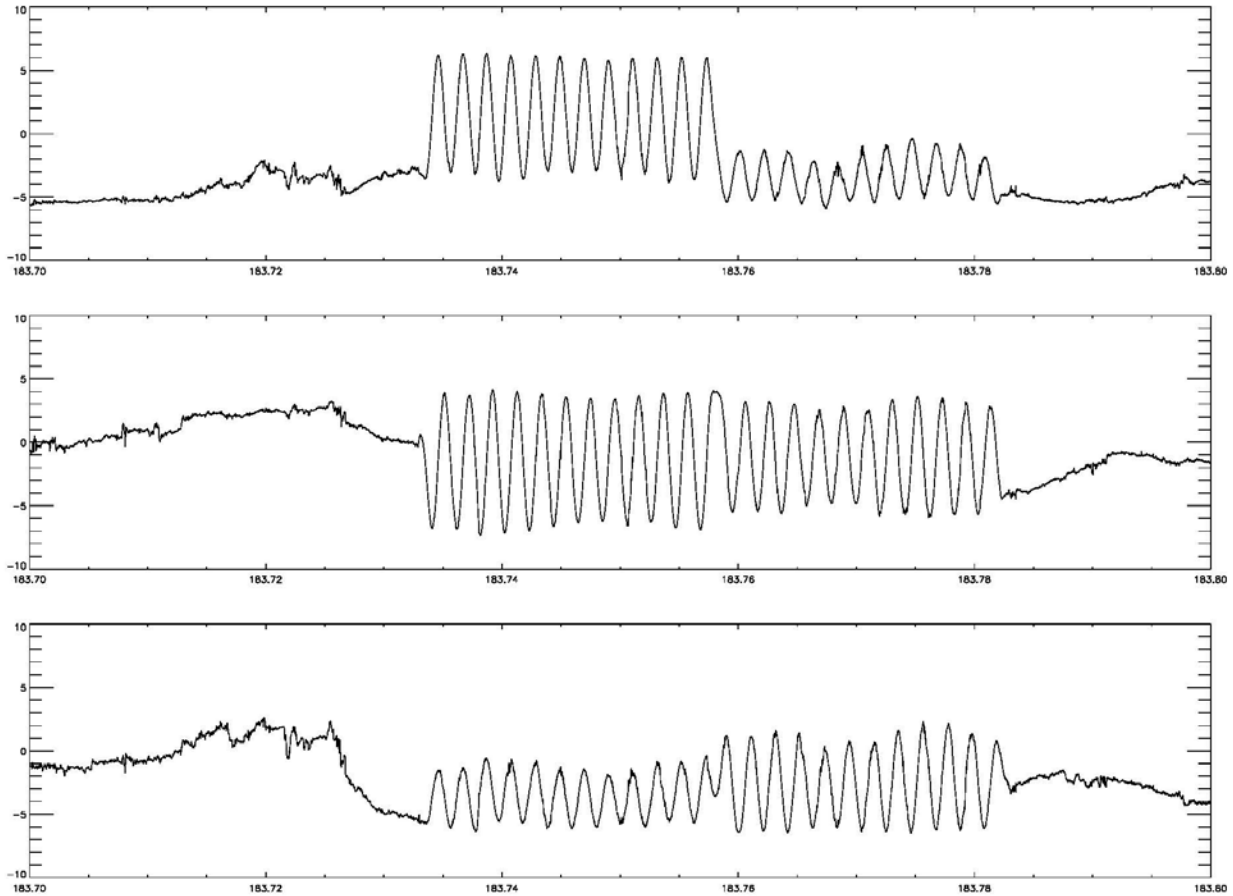
1254

1255

1256　Figure 17: Magnetic field in spacecraft payload coordinates throughout the second cruise MAGROLL

1257　maneuver on DOY 183, 2014, during which the spacecraft executes a rolls at 2 degrees/s about a

1258　principal axis (near the z axis), followed by rolls about an orthogonal axis (near spacecraft x).

1259　Instrument dynamic range was commanded to manual range 1 (+/- 2048 nT) for the first few rolls about

1260　z, followed by rolls about both z and x in range 0 (+/- 512 nT), followed by rolls about x in range 1.

1261　After completion of the sequence, the instruments are returned to autorange mode.
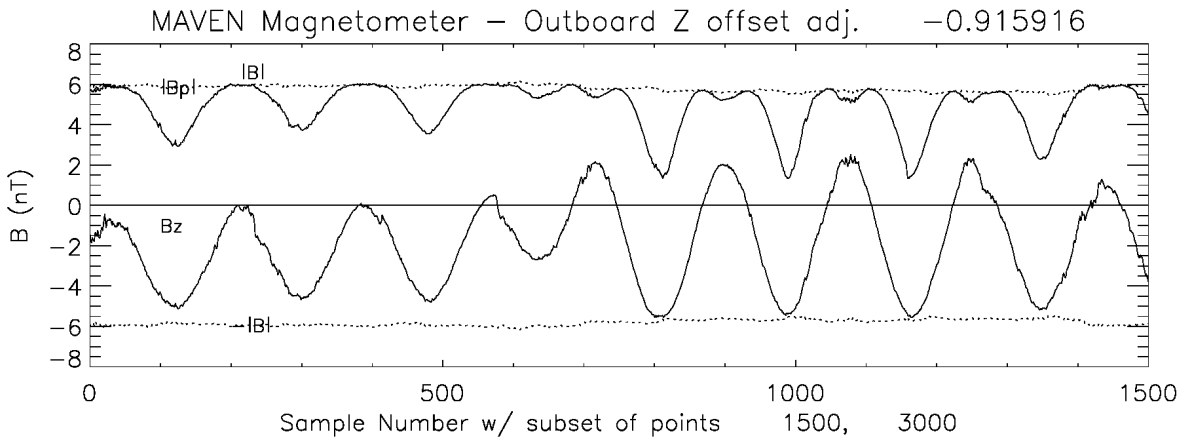
1262

1263

MAVEN Magnetometer — Outboard
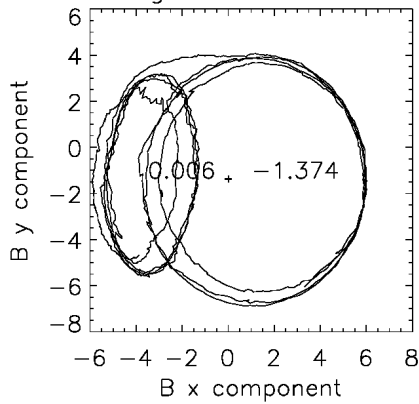
X offset =   0.006

Y offset =   −1.374

Z offset =   −0.916

  range =   0

LAG = 6 seconds

Z offset corrected

magroll_2_pl_sunsc.sts

MAVEN Magnetometer — Outboard Z offset adj.   −0.915916

1264   magroll_2_pl_sunsc.sts

1265

1266   Figure 18: Application of offset estimation to range 0 (+/- 512 nT range) observations obtained during

1267   the second cruise magroll exercise, using a six second lag for vector differences, during which the field

1268   rotates in the sc reference frame by 12 degrees. The figure in the upper left is a diagnostic hodogram of

1269 B_y vs B_x. In the lower figure a time series of the field magnitude and the negative of the field magnitude

1270   is shown (dotted line) demonstrating little spin modulation with the estimated offsets applied to the

1271   vector observations.

56

MAG Preliminary Processing
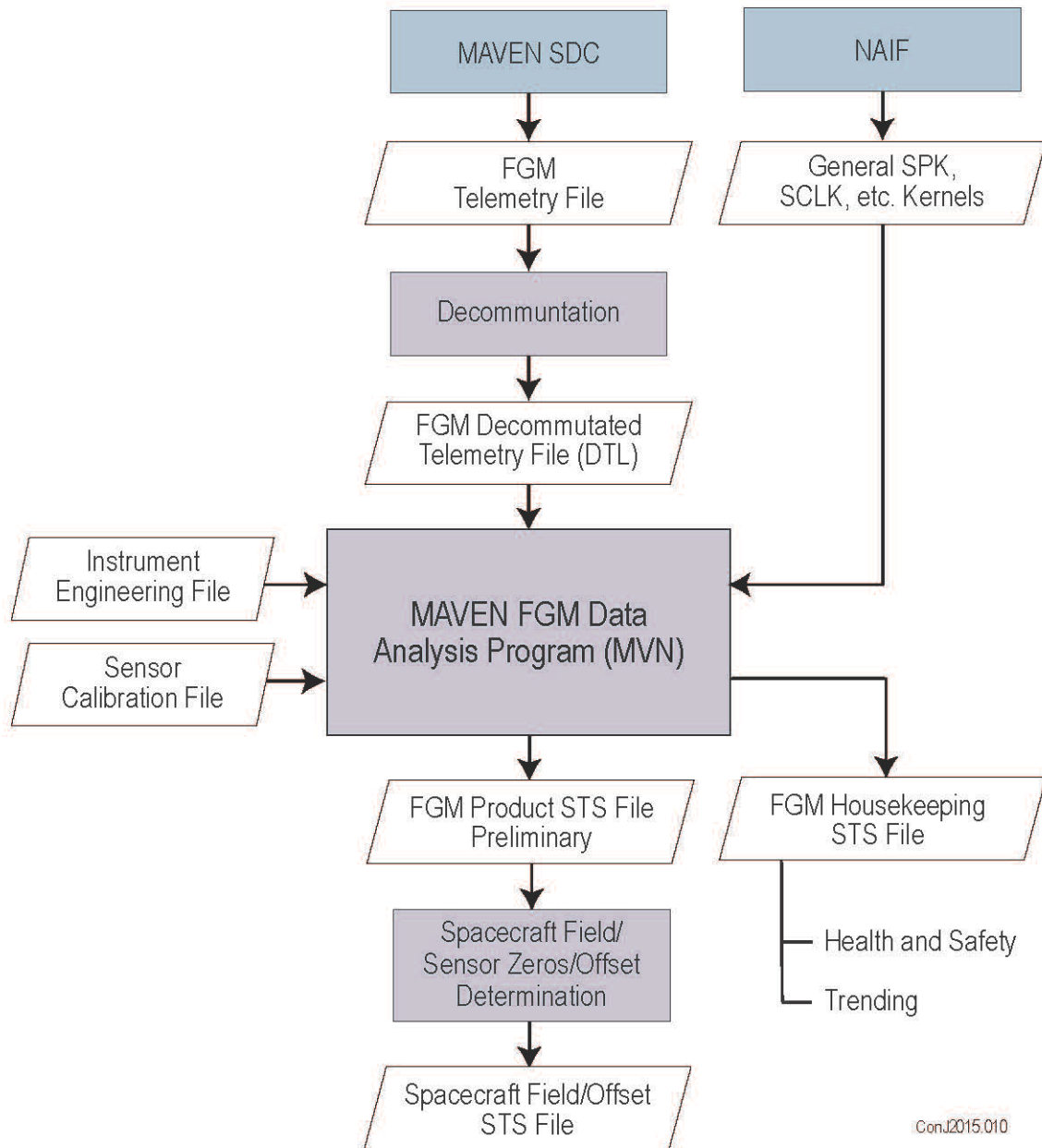
Figure 19: Flow diagram of the preliminary MAG data processing. Preliminary processing is done prior to receipt of supplementary spacecraft engineering data (e.g., solar array currents), reconstructed spacecraft ephemeris, and attitude kernels, to assess instrument health and safety and to estimate sensor zeros and/or static spacecraft magnetic fields.
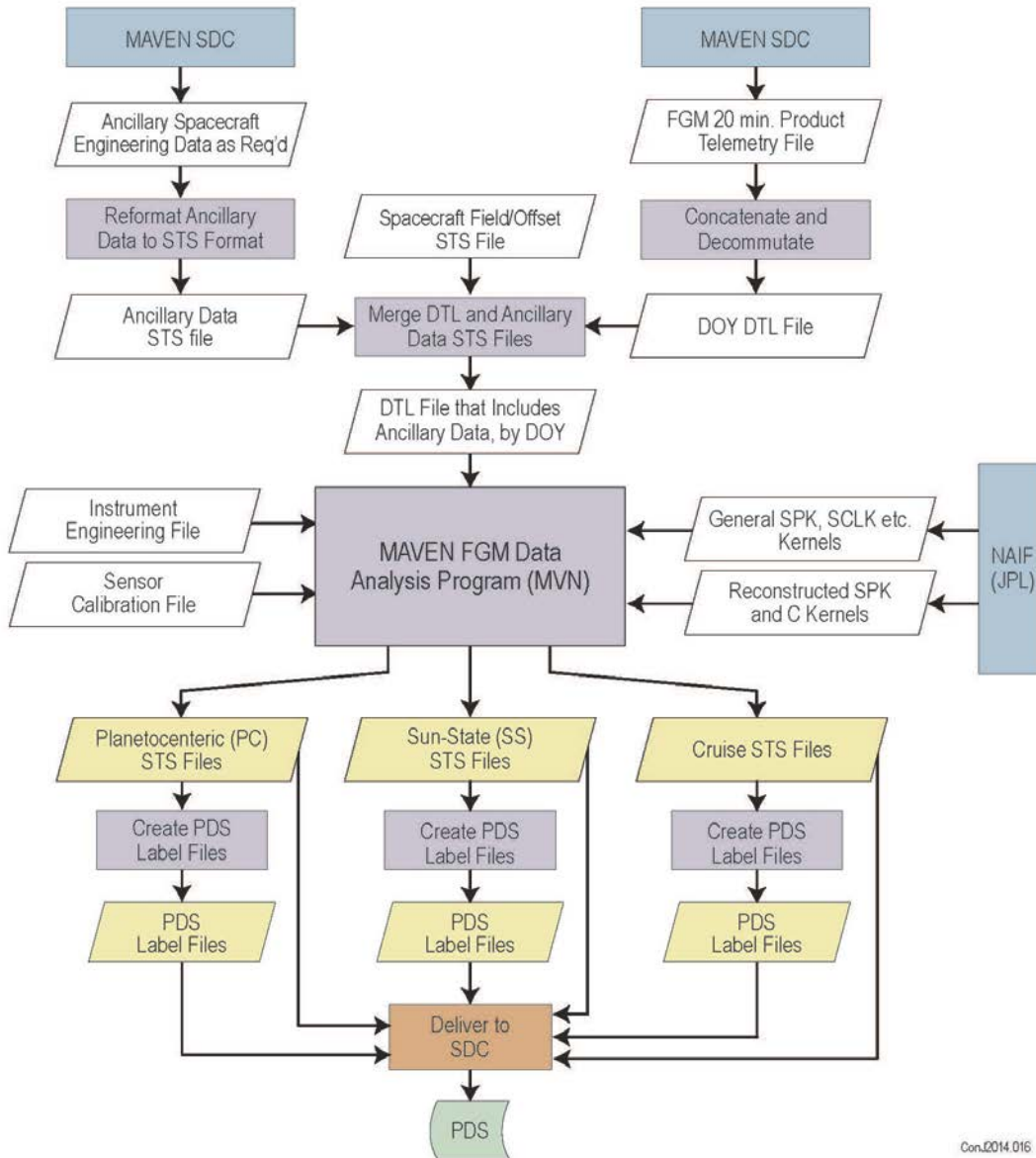
Figure 20: Flow diagram of MAG final data processing. Final processing is done subsequent to receipt of reconstructed spacecraft ephemeris and attitude kernels using the same program elements. Data files containing time-ordered records of fully-calibrated magnetic field vectors, rendered in several useful coordinate systems, are the archive data products. Each record contains spacecraft position rendered in the appropriate coordinate system along with supplementary engineering data, where useful.